Hyperdeformation in the cranked relativistic mean field theory: The $Z = 40$–58 region of the nuclear chart

A. V. Afanasjev and H. Abusara
Department of Physics and Astronomy, Mississippi State University, Mississippi 39762, USA
(Received 17 April 2008; published 23 July 2008)

The systematic investigation of hyperdeformation (HD) at high spin in the $Z = 40 - 58$ region of the nuclear chart was performed in the framework of the cranked relativistic mean-field theory. The properties of the moments of inertia of the HD bands, the role of the single-particle and necking degrees of freedom at HD, the spins at which the HD bands become yrast, the possibility to observe discrete HD bands, and so on are discussed in detail.

DOI: 10.1103/PhysRevC.78.014315 PACS number(s): 21.60.Jz, 27.50.+e, 27.60.+j, 21.10.Ft

I. INTRODUCTION

Since the discovery of superdeformation (SD) in ^{152}Dy two decades ago [1], nuclear SD has been in the focus of attention of the nuclear structure community; it has been discovered in different mass regions and extensively studied experimentally [2] and theoretically (see, for example, Refs. [3–5] and references therein). New phenomena such as identical bands [3] were discovered, and the rich variety of experimental data allowed us to test modern theoretical tools under extreme conditions of large deformation and fast rotation.

It was known for a long time from harmonic oscillator studies [6] that even more elongated shapes, called as hyperdeformed (HD) and characterized by the semiaxis ratio of around 3:1, are possible. The existence of such stable shapes was later confirmed in the macroscopic+microscopic (MM) method [7–15]. Theoretical results on the states located in third (HD) minima are also available in self-consistent Hartree-Fock+Bogoliubov (HFB) approaches based on the Skyrme and Gogny forces (see Refs. [16–18] and references quoted therein), and relativistic mean-field approach [19]. However, these results are restricted to spin-zero states, which are difficult to measure in experiment. To our knowledge, the description of the HD states at high spin within the self-consistent approach has been attempted only in ^{108}Cd [20] within the cranked relativistic mean-field (CRMF) method] and in four $A \sim 40$ mass nuclei [21] (within the cranked Skyrme-Hartree-Fock approach). The general feature of all these calculations is the fact that the semiaxis ratio of the HD shapes is less than 3:1 [5].

Let us mention two examples of such studies: one at spin zero and another at high spin. In actinide nuclei, the HD states are so-called third minima states around ^{232}Th [11,22,23]. In these nuclei, the second saddle point is split, leading to the excited reflection-symmetric and reflection asymmetric configurations with large quadrupole and octupole deformations, $\beta_2 \sim 0.9$ and $\beta_3 \sim 0.35$. The density distribution at the HD minimum resembles a di-nucleus consisting of a nearly spherical nucleus around the doubly magic nucleus ^{132}Sn and a well-deformed fragment from the neutron-rich $A \sim 100$ region [11]. Unfortunately, it is very difficult to study the HD states at low spin in experiment. To overcome this problem, one should use the fact that the larger moment of inertia connected with the larger deformation drives the nucleus toward larger deformations with increasing angular momentum; the HD minimum is thus favored by rotation and becomes ultimately yrast at high spin. For example, cranked Nilsson-Strutinsky calculations suggested the existence of very elongated high-spin minima in nuclei around ^{168}Yb [9]. These HD bands are expected to become yrast at spin around $80\hbar$.

On the experimental side, very little was known about hyperdeformation apart from some indications of this phenomenon at low spin in the uranium nuclei [24] and light nuclei like ^{12}C [25] and the observation of the HD ridge structures at high spin in the $A \sim 150$ mass region [26,27]. Recent observation of the very extended shapes in ^{108}Cd [28,29], strongly motivated by earlier calculations of Ref. [12] and more recent studies of Ref. [15], has renewed interest in the study of hyperdeformation at high spin. Although the hyperdeformed nature of the bands in this nucleus has not been confirmed in the subsequent cranked relativistic mean-field analysis of Ref. [20] (see also Sect. VB in Ref. [30]), this experiment provided a strong motivation for subsequent experimental searches in the $A \sim 125$ mass region (see Refs. [31–33]) and theoretical studies of Refs. [5,30] within the framework of the MM method. These experiments revealed rotational patterns in the form of ridge-structures in three-dimensional (3D) rotational mapped spectra with dynamic moments of inertia $J^{(2)}$ ranging from 63 to 111 MeV^{-1} in 12 different nuclei [31]; the values around 110 MeV^{-1} observed in ^{118}Te, ^{124}Xe, and ^{124,125}Cs suggest that the HD structures were populated in these experiments. However, no discrete rotational HD bands have been identified. It is also necessary to mention that several previous attempts to search for high spin HD structures in ^{147}Gd [34,35], ^{152}Dy [26,27], and ^{168}Yb [36] did not lead to convincing evidences for discrete HD bands.

So far, theoretical investigations of HD at high spin were carried out mainly in the framework of the MM method. One of the main goals of the current manuscript is to perform for the first time a systematic study of HD within the framework of fully self-consistent theory, the CRMF theory. Figure 1 shows the part of the nuclear chart where our studies are performed. We restrict our investigation to even-even nuclei; the only exceptions are odd-mass nuclei ^{111}I (in which extremely SD doubly magic band has been found) and ^{123,124}Xe, ^{123}I and ^{125}Cs (which are used in the study of the relative properties of the HD bands). In each isotope chain we consider nuclei

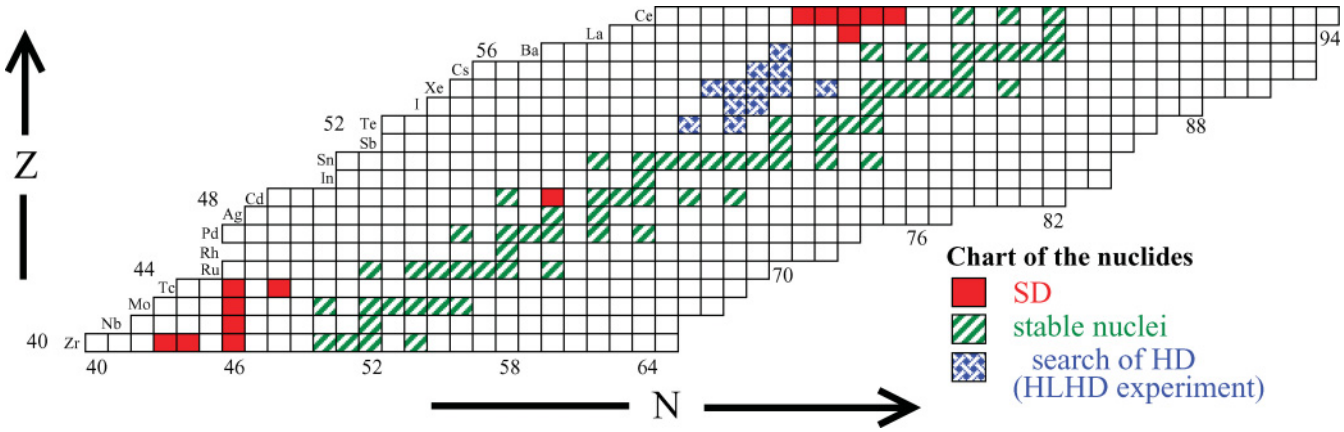

FIG. 1. (Color online) The chart of nuclei in the $Z = 40$–58 region. Only experimentally known nuclei are shown. Experimental data on superdeformed nuclei are taken from Ref. [2]. The nuclei in which the search for HD structures has been performed in the HLHD experiment are taken from Ref. [31].

ranging from the most proton-rich ones up to the ones located at the neutron-rich side of the β-stability valley. Neutron-rich nuclei beyond the valley of the β stability are excluded from consideration because of the experimental difficulties of studying them at high spins relevant for HD. With the goal to guide future experimental explorations and to find the nuclei in which the HD may be studied with current and future experimental facilities, we define the spins at which the HD bands become yrast in these nuclei. In addition, available experimental data on the HD ridge structures in the Te, Xe, and Cs nuclei are analyzed. The general features of the HD bands are outlined.

The role of the single-particle degrees of freedom at hyperdeformation has not been studied in detail till now. One of the major goals of the current manuscript is the study of their role, and it is motivated by the desire to understand to what extent theoretical methods developed in the study of the SD bands are also applicable to the HD bands. It is very unlikely that the spins, parities, and excitations energies of the HD bands will be known in the initial stage of their experimental study. The direct test of the structure of the wave functions of the single-nucleonic orbitals (e.g., via magnetic moments) will also not be possible at that stage. Thus, similar to the case of superdeformation [3,37–39], the relative properties of different HD bands may play an important role in the interpretation of their structure. In this context, it is important to understand which changes of the single-particle orbitals are involved in going from one HD band to another, and how they affect physical observables like dynamic moments of inertia $J^{(2)}$, transition quadrupole moments Q_t, total spin I, etc. In particular, we will study whether the theoretical methods that were systematically used in the configuration assignment of the SD bands are also applicable to the HD bands. These include the methods based on the relative properties of the dynamic moments of inertia $J^{(2)}$ [3,37], on the effective alignments $i_{\rm eff}$ [3,38,39] and on the relative transition quadrupole moments ΔQ_t [40,41].

The manuscript is organized as follows. The definition of physical observables and the details of numerical calculations are discussed in Sec. II. The spins at which the HD bands become yrast, the regions of nuclear chart where the experimental search for the HD structures may be successful, and the general properties of the HD bands are outlined in Sec. III. The data obtained in the search of the HD structures in the $A \sim 120$ mass region and the single-particle degrees of freedom are also analysed in this section. Section IV is devoted to the analysis of extremely superdeformed (ESD) structure in ^{111}I. The calculations predict the existence of doubly magic ESD structure in this nucleus with the deformations being close to HD, which may be observed with the current generation of γ-ray detectors. Finally, Sec. V contains the main conclusions of our work.

II. THE DETAILS OF THE CALCULATIONS

In the relativistic mean-field (RMF) theory the nucleus is described as a system of pointlike nucleons, Dirac spinors, coupled to mesons and to the photons [42–44]. The nucleons interact by the exchange of several mesons, namely a scalar meson σ and three vector particles, ω, ρ, and the photon. The CRMF theory [4,45–47] represents the extension of RMF theory to the rotating frame. It has successfully been tested in a systematic way on the properties of different types of rotational bands in the regime of weak pairing such as normal-deformed [48], superdeformed [4,49], as well as smooth terminating bands [44].

In the current study, we restrict ourselves to reflection symmetric shapes since previous calculations in the MM method show no indications that odd-multipole (octupole, ...) deformations play a role in the SD and HD bands of the nuclei covered by our study [15] and in the HD bands of the $A \sim 110$–125 [50] mass region.

A. Physical observables

Similar to the case of the SD bands, it is reasonable to expect that the HD bands will not be linked to the low-spin level scheme for a long period of time. Thus, the spins and parities of the HD bands will not be known and it will not be possible to define the kinematic moment of inertia $J^{(1)}$ because

it depends on the absolute values of the spin. In such a situation, the dynamic moment of inertia $J^{(2)}$ will play an important role in our understanding of the structure of the HD bands. This is similar to the case of the SD bands (see Refs. [3,37]). Other observables, such as transition quadrupole moments Q_t and effective (relative) alignments $i_{\rm eff}$, will also be important.

In the CRMF calculations, the rotational frequency Ω_x, the kinematic moment of inertia $J^{(1)}$ and the dynamic moment of inertia $J^{(2)}$ are defined by

$$\Omega_x = \frac{dE}{dJ}, \tag{1}$$

$$J^{(1)}(\Omega_x) = J\left\{\frac{dE}{dJ}\right\}^{-1}, \tag{2}$$

$$J^{(2)}(\Omega_x) = \left\{\frac{d^2E}{dJ^2}\right\}^{-1}. \tag{3}$$

The charge quadrupole Q_0 and mass hexadecupole Q_{40} moments are calculated by using the expressions

$$Q_0 = e\sqrt{\frac{16\pi}{5}}\sqrt{\langle r^2Y_{20}\rangle_p^2 + 2\langle r^2Y_{22}\rangle_p^2}, \tag{4}$$

$$Q_{40} = \langle r^4Y_{40}\rangle_p + \langle r^4Y_{40}\rangle_n, \tag{5}$$

where the labels p and n are used for protons and neutrons, respectively, and e is the electrical charge. At axially symmetric shapes, typical for the hyperdeformed states, the transition quadrupole moment Q_t is equal to Q_0.

The quadrupole deformation β_2 for axially symmetric shapes is frequently defined in self-consistent calculations from calculated and/or experimental quadrupole moments using simple relation [18,51,53]

$$\beta_2 = \frac{1}{XR^2}\sqrt{\frac{5\pi}{9}}Q_0^X, \tag{6}$$

where $R = 1.2A^{1/3}$ fm is the radius of the nucleus and Q_0^X is a quadrupole moment of the X-th (sub)system expressed in fm^2. Here X refers either to proton ($X = Z$) or neutron ($X = N$) subsystem or represents total nuclear system ($X = A$). This expression, however, neglects the higher powers of β_2 and higher multipolarity deformations $\beta_4, \beta_6, \ldots$ [54], which play an important role at hyperdeformation.

Considering that the definition of the deformation is model dependent [54], and that this quantity is not experimentally measurable, we prefer to use transition quadrupole moment Q_t for the description of deformation properties of hyperdeformed states. This is experimentally measurable quantity, so in the future our predictions can be directly compared with experiment. The deformation properties of the yrast SD band in ^{152}Dy (which is one of the most deformed SD bands [28]) are used as a reference. This is done by introducing normalized transition quadrupole moment $Q_t^{\rm norm}(Z, A)$ in the (Z, A) system

$$Q_t^{\rm norm}(Z, A) = \frac{ZA^{2/3}}{100.36}\ e{\rm b} \tag{7}$$

This equation is based on the ratio $Q_t^{\rm norm}(Z, A)/Q_t(^{152}{\rm Dy})$ calculated using Eq. (6) under the assumption that the β_2 values in the (Z, A) system and in ^{152}Dy are the same. We use the value $Q_t(^{152}{\rm Dy}) = 18.73\ e$b obtained in the CRMF calculations with the NL1 parametrization of the RMF Lagrangian for the yrast SD band in ^{152}Dy at $I = 60\hbar$ in Ref. [4]. Thus, in first approximation (neglecting the higher powers of β_2 and higher multipolarity deformations $\beta_4, \beta_6, \ldots$) the equilibrium deformation of the band in the (Z, A) system having the $Q_t^{\rm norm}(Z, A)$ value is the same as in the yrast SD band of ^{152}Dy. We describe the band as hyperdeformed if its Q_t value exceeds $Q_t^{\rm norm}(Z, A)$ by at least 40%. This criteria is somewhat relaxed in the $Z = 40,\ 42,\ 44$ nuclei for which the band is defined as HD if its Q_t value exceeds $Q_t^{\rm norm}(Z, A)$ by at least 30%.

The effective (relative) alignment $i_{\rm eff}$ between two bands is defined as the difference between the spins of two levels in bands A and B at the same rotational frequency Ω_x [38]:

$$i_{\rm eff}^{B,A}(\Omega_x) = I_B(\Omega_x) - I_A(\Omega_x). \tag{8}$$

This quantity has been used frequently in the analysis of the single-particle structure of the SD bands and the configuration assignment (see Refs. [38,39] and references quoted therein). It depends on both the alignment properties of the single-particle orbital(s) by which the two bands differ and the polarization effects induced by the particles in these orbitals [52]. The latter are in part related to nuclear magnetism.

Because the pairing correlations are relatively weak in the HD bands of interest (see Sec. III C), their intrinsic structure can be described by means of the dominant single-particle components of the hyperintruder states occupied. The calculated configurations will be labeled by $[p, n_1n_2]$, where p, n_1, and n_2 are the number of proton $N = 7$ and neutron $N = 7$ and $N = 8$ hyperintruder orbitals occupied, respectively. For most of the HD configurations, neutron $N = 8$ orbitals are not occupied, so the label n_2 will be omitted in the labeling of such configurations.

Single-particle orbitals are labeled by $[Nn_z\Lambda]\Omega^{\rm sign}$. $[Nn_z\Lambda]\Omega$ are the asymptotic quantum numbers (Nilsson quantum numbers) of the dominant component of the wave function at $\Omega_x = 0.0$ MeV. The superscripts *sign* to the orbital labels are used to indicate the sign of the signature r for that orbital ($r = \pm i$).

The spins at which the SD and HD configurations become yrast in the calculations are defined as crossing spins $I_{\rm cr}^{\rm SD}$ and $I_{\rm cr}^{\rm HD}$, respectively.

B. Numerical scheme of the CRMF calculations

The CRMF equations are solved in the basis of an anisotropic three-dimensional harmonic oscillator in Cartesian coordinates characterized by the deformation parameters β_0 and γ and oscillator frequency $\hbar\omega_0 = 41A^{-1/3}$ MeV, for details see Refs. [4,45]. The truncation of basis is performed in such a way that all states belonging to the shells up to fermionic N_F and bosonic N_B are taken into account.

The impact of the truncation of basis on the numerical accuracy of the calculations has first been studied in the axially symmetric RMF code, see Fig. 2. In the mass region of interest, the calculations with $N_F = 12$ provide a reasonable approximation to the fully convergent $N_F = 26$ solution up

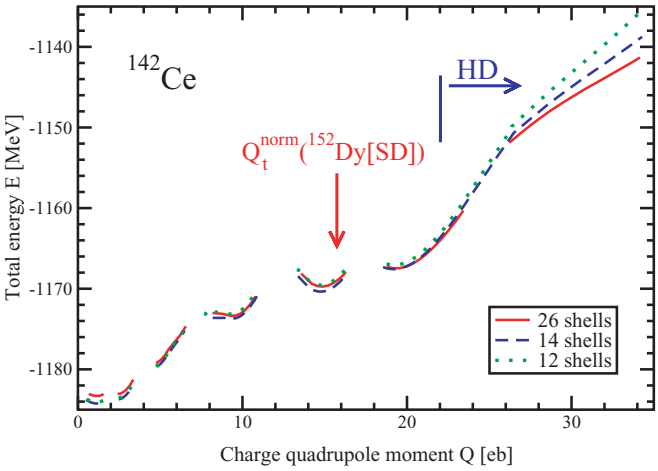

FIG. 2. (Color online) Potential energy surfaces (PES) obtained in the axially symmetric RMF calculations without pairing in the ^{142}Ce nucleus. The results of calculations with $N_F = 12$, 14, and 26 are shown. In all these calculations, N_B is fixed at 26. The results with $N_F = 26$ correspond to a fully converged solution: the binding energies do not change with further increase of N_F. The gaps in the PES lines are due to jumps of the solution from one single-particle configuration to another. The same single-particle configurations are compared at the same value of charge quadrupole moment. The normalized value of transition quadrupole moment $Q_t^{\rm norm}$ corresponding to the deformation of the yrast SD band in ^{152}Dy is indicated by arrow. The range of hyperdeformation is also indicated.

to a deformation typical for the SD shapes. However, this truncation scheme becomes a poor approximation when the quadrupole moment appreciably exceeds the one corresponding to the lower limit of HD; the difference between the $N_F = 12$ and $N_F = 26$ solutions increases rapidly with the increase of quadrupole moment (see Fig. 2). However, in this quadrupole moment range the results of the calculations with $N_F = 14$ are closer to exact solution, although still exceeding it by ∼1–2 MeV at the upper end of the calculated quadrupole moment range. It was tested that with the decrease of the mass, the difference between the $N_F = 14$ and $N_F = 26$ solutions will also decrease as well so the difference falls within the range of 1 MeV for the majority of the nuclei under study.

These conclusions have also been tested in triaxial CRMF calculations. It was concluded that physical observables of interest are described with sufficient numerical accuracy when $N_F = 12$ is used for the SD and ND states and $N_F = 14$ for the HD states. Thus, we employ a hybrid calculational scheme in which the CRMF solutions in the ND and SD minima are sought using $N_F = 12$, whereas the ones in the HD minima using $N_F = 14$. In all CRMF calculations, we use $N_B = 20$. To eliminate the numerical inaccuracies in the definition of the crossing spin $I_{\rm cr}^{\rm HD}$, the yrast ND/SD configurations, which are crossed by the yrast HD configuration, were recalculated in the crossing region using $N_F = 14$, and only then the crossing spin was defined. One should keep in mind that even with $N_F = 14$ the spins at which the HD configurations become yrast in the calculations may be overestimated by 1–2$\hbar$ when the deformation of the HD configurations exceeds appreciably the one corresponding to the lower limit of HD.

When searching for different types of rotational structures it is important to find the solutions in all local minima which are close to the yrast line to properly define the crossing spins between the rotational structures of different nature. This is easily achievable in the macroscopic+microscopic approach by creating potential energy surfaces (PES) in the deformation space covering quadrupole and triaxial deformations [12,55]. However, the computational cost to create similar PES in the self-consistent models is enormous, thus it has never been attempted in rotating nuclei. To overcome this problem, we use the fact that in self-consistent approaches without pairing the deformation of the basis defines to a large extent the local minima where the solutions will be obtained. Thus, the solutions in the ND minima, including triaxial ones, are searched using three combinations of the deformation of basis: $(\beta_0 = 0.30, \gamma = -30^\circ)$, $(\beta_0 = 0.30, \gamma = 0^\circ)$, and $(\beta_0 = 0.30, \gamma = +30^\circ)$. In a similar way, the solutions in the SD minima are searched using the following combinations of the deformations of basis $(\beta_0 = 0.65, \gamma = -30^\circ)$, $(\beta_0 = 0.65, \gamma = 0^\circ)$, $(\beta_0 = 0.65, \gamma = +30^\circ)$, and $(\beta_0 = 0.8, \gamma = 0^\circ)$. The latter deformation of basis also leads frequently to the HD solutions. The deformation of basis $(\beta_0 = 1.0, \gamma = 0^\circ)$ has been used for the search of the solutions in the HD minima. Nonzero γ deformations of basis at large β_0 lead either to the same solution as $\gamma = 0^\circ$ or to the highly excited configurations. For each of the above-mentioned values of the deformation of basis, the lowest in energy solutions are calculated as a function of spin, and the yrast line is formed from these solutions.

C. The selection of the RMF parametrization

The NL1 parametrization of the RMF Lagrangian [56] is used in the majority of the calculations in the current manuscript. As follows from previous studies, this parametrization provides a good description of the moments of inertia of the rotational bands in unpaired regime in the SD and ND minima [4,39,44,49], the single-particle energies for the nuclei around the valley of β stability [39,51], and the excitation energies of the SD minima [57]. NL3 [58] is an alternative parametrization, the quality of which has been tested in rotating nuclei (but less extensively than in the case of NL1) [39,48,49,59]. Some results with this parametrization will be presented. Few results obtained with the NLSH [60] and NLZ [61] parametrizations will be shown in Sec. III C to illustrate the possible spread of calculated quantities. It is necessary to keep in mind that the quality of the NLSH parametrization in respect of the description of rotational properties of the nuclei as well as their single-particle energies is not as good as that of the NL1 and NL3 [39,49,51], and the force NLZ has not been tested in that respect.

The spins at which the rotational structures belonging to different minima in potential energy surfaces become yrast depend in general on the relative energies of these minima and on the moments of inertia of rotational structures in these minima. Previous experience shows that different parametrizations of the RMF Lagrangian give similar moments of inertia for the same configuration [39,44,49,59] (see also Fig. 13 below). Figure 3 also illustrates that the potential energy surfaces at spin zero as a function of charge quadrupole moment

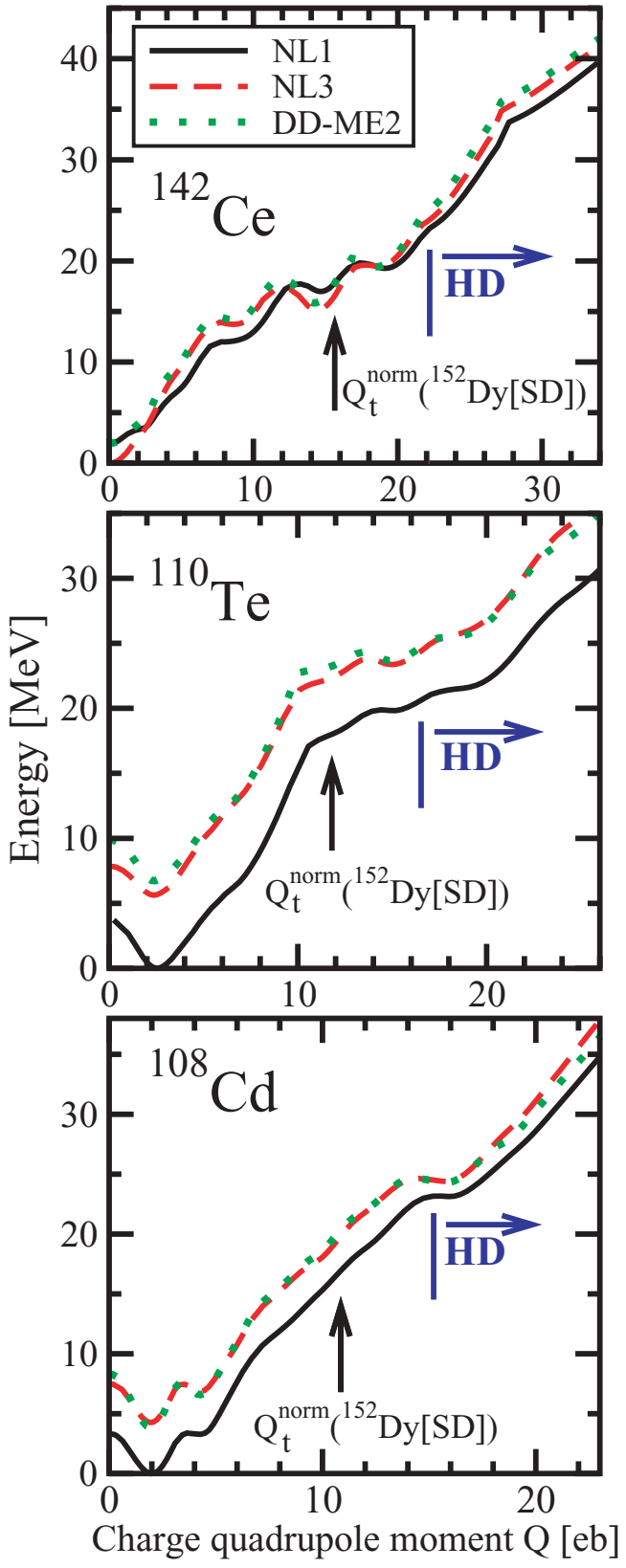

FIG. 3. (Color online) The same as in Fig. 2 but for the results obtained in the axially symmetric RMF calculations with pairing using different parametrizations of the RMF Lagrangian and $N_F = 26$. Figure shows the binding energies normalized with respect to the lowest energy of the lowest potential energy curve.

obtained with the NL1 and NL3 parametrizations are similar in shape. These two facts suggest that the HD configurations should become yrast at approximately the same spins in both parametrizations: this conclusion is confirmed in Sec. III A. It is interesting to note that the NL3 curve in Fig. 3 is similar to the one obtained with recently developed density-dependent meson-exchange effective interaction DD-ME2 [62], which represents a new class of the RMF parametrizations as compared with NL1 and NL3. However, so far this interaction has not been used in the studies of rotating nuclei, thus it is not employed in the current study because its reliability in the description of rotational properties is not known.

III. HYPERDEFORMATION AT HIGH SPIN: WHERE TO EXPECT AND ITS GENERAL FEATURES

A. The systematics of crossing spins and transition quadrupole moments of the HD bands

Figures 4–7 display the spins at which the SD and HD configurations become yrast (crossing spins) in the CRMF calculations. In addition, the calculated transition quadrupole moments of these configurations at spin values close to the crossing spins are shown. The calculated HD configurations are near-prolate. One can see that the crossing spins I_{cr}^{HD} are typically lower for proton-rich nuclei. Such a feature is seen in most of the isotope chains; by going from the β stability valley toward the proton drip line, one can lower I_{cr}^{HD} by approximately $10\hbar$. The minimum of crossing spins I_{cr}^{HD} is reached at $N \approx Z + 10$ in the Pd, Te, and Ru isotope chains [see Figs. 5(e), 5(a), and 7(a)], and the Mo isotope chain [Fig. 7(c)] shows almost no dependence of I_{cr}^{HD} on mass number. In other isotope chains, the minima in crossing spins I_{cr}^{HD} appear in most proton-rich nuclei. Considering that the sensitivity of modern γ-ray detectors allows study of discrete rotational bands only up to $\approx 65\hbar$ in medium mass nuclei [63–65], and that the observation of higher spin states will most likely require a new generation of γ-ray tracking detectors such as GRETA or AGATA, these features of crossing spins I_{cr}^{HD} represent an important constraint.

As suggested by the studies of the Jacobi shape transition in Ref. [30], the coexistence of the SD and HD minima at the feeding spins may have an impact on the survival of the HD minima because of the decay from the HD to SD configurations. If this mechanism is active, then only the nuclei in which the HD minimum is lower in energy than the SD one at the feeding spin and/or the nuclei characterized by the large barrier between the HD and SD minima will be the reasonable candidates for a search of the HD bands. Figures 4–7 show that the HD configurations become yrast at lower spin than the SD ones only in a specific mass range that depends on the isotope chain. This range can be narrow as in the case of Te isotopes [Fig. 5(a)] or wide as in the case of Ce isotopes [Fig. 4(a)]. The question of the population of the HD bands within the RMF framework definitely deserves an additional study, but such a study is beyond the scope of the present manuscript.

Figure 6 compares the results of the calculations for Cd isotopes obtained with the NL1 and NL3 parametrizations of the RMF Lagrangian. One can see that both parametrizations predict similar crossing spins I_{cr}^{SD} and I_{cr}^{HD} and similar

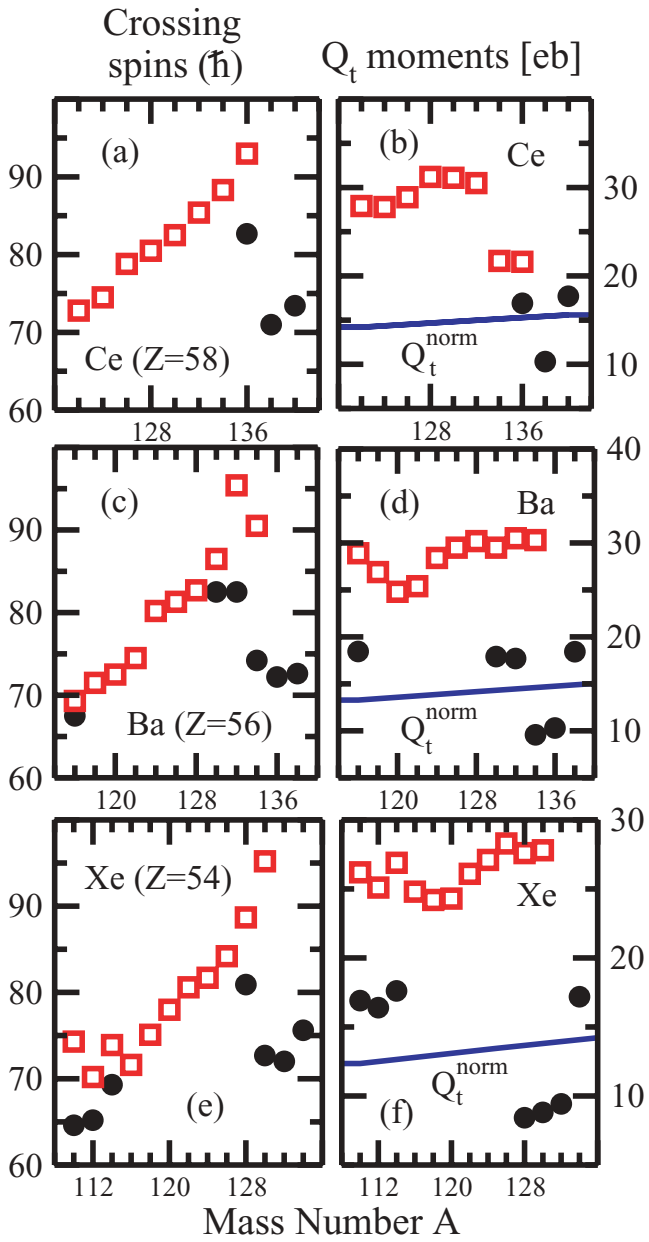

FIG. 4. (Color online) The crossing spins (left panels) at which the SD (solid circles) and HD (open squares) configurations become yrast and their transition quadrupole moments Q_t (right panels) for the Ce, Ba, and Xe isotopes. The values for the SD configurations are shown only in the cases when they become yrast at lower spins than the HD configurations. The normalized transition quadrupole moments $Q_t^{\rm norm}$ corresponding to the deformation of the yrast SD band in ^{152}Dy are also shown.

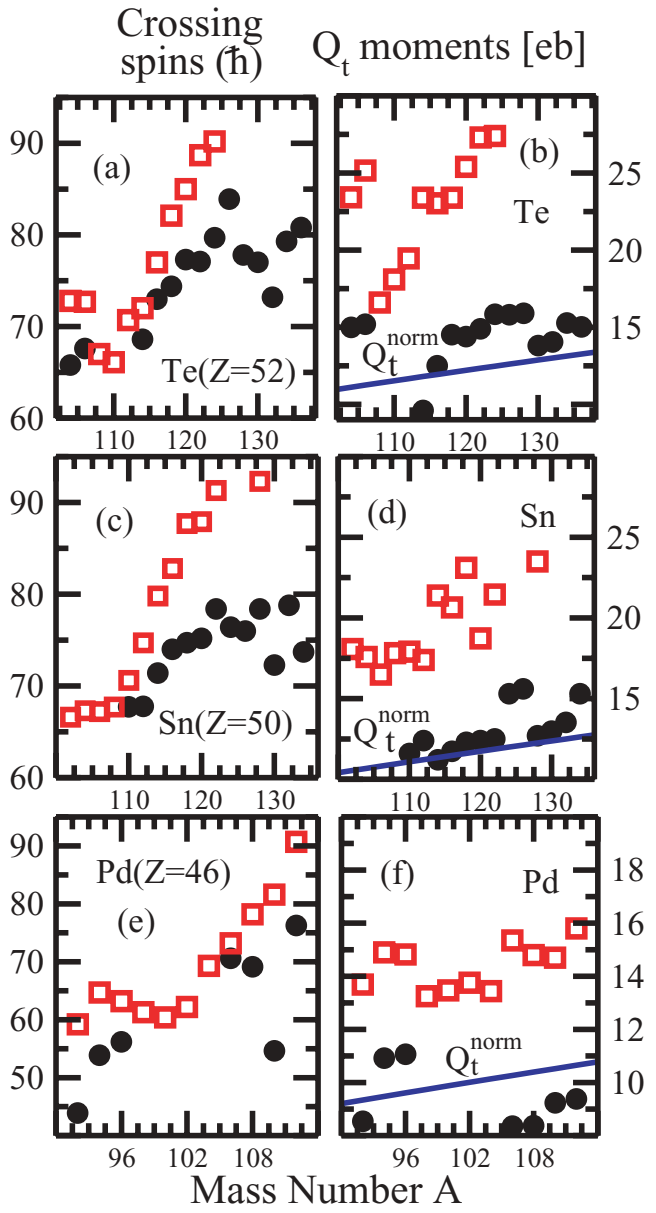

FIG. 5. (Color online) The same as in Fig. 4 but for the Te, Sn, and Pd isotopes.

transition quadrupole moments. However, in average, the crossing spins $I_{\rm cr}^{\rm HD}$ calculated with NL3 are somewhat lower (by 1–2$\hbar$) than the ones obtained in the calculations with NL1.

B. The $A \sim 120$ region: the analysis of experimental data

The recent Hyper-Long-HyperDeformed (HLHD) experiment at the EUROBALL-IV γ-detector array revealed some features expected for HD nuclei [31–33]. Although no discrete HD rotational bands have been identified, rotational patterns in the form of ridge-structures in three-dimensional (3D) rotational mapped spectra are identified with dynamic moments of inertia $J^{(2)}$ ranging from 71 to 111 MeV^{-1} in 12 different nuclei selected by charged-particle and/or γ gating (see Table I). The four nuclei, ^{118}Te, ^{124}Cs, ^{125}Cs, and ^{124}Xe, found with moment of inertia $J^{(2)} \sim 110$ MeV^{-1} are most likely hyperdeformed,[1] whereas the remaining nuclei with smaller values of $J^{(2)}$ are expected to be superdeformed. The width in energy of the observed ridges indicates that there are ≈6–10 transitions in the HD cascades, and a fluctuation analysis shows

[1]For comparison, the HD ridges in ^{152}Dy are characterized by $J^{(2)} \sim 130$ MeV^{-1} [27].

TABLE I. The values of the dynamic moment of inertia $J^{(2)}_{\rm exp}$ of ridge structures measured in the HLHD experiment [31]. Theoretical results obtained in the MM calculations [30] are shown in the last column.

Nucleus	$J^{(2)}_{\rm exp}$	$J^{(2)}_{\rm MM}$
^{126}Ba	77	118
^{123}Xe	71	
^{122}Xe	77	108
^{121}Xe	63	
^{120}Te	71	
^{118}Te	111	97
^{125}Cs	100	106
^{124}Cs	111	
^{124}Xe	111	111
^{122}I	71	
^{121}I	77	102
^{126}Xe	83	110

that the number of bands in the ridges exceeds 10. The HD ridges are observed in the frequency range of about 650 to 800 keV, and their dynamic moments of inertia have typical uncertainty of 10% (e.g., 111 $\pm$ 11 MeV^{-1} in ^{124}Xe) [66].

The experimental data show unusual features never before seen in the studies of the SD bands. For example, the addition of one neutron on going from ^{124}Cs to ^{125}Cs decreases the experimental $J^{(2)}$ value by $\sim$10% (from 111 MeV^{-1} down to 100 MeV^{-1}; see Table I). A similar situation is also seen in the SD minimum: the addition of one neutron on going from ^{121}Xe to ^{122}Xe increases the experimental $J^{(2)}$ value by $\sim$22% (from 63 MeV^{-1} to 77 MeV^{-1}; see Table I). It is impossible to find an explanation for such a big impact of the single particle on the properties of nuclei: previous studies in the SD minima in different parts of the nuclear chart never showed such features. The case of the pair of ^{123}Xe and ^{124}Xe is even more intriguing: a single particle triggers the transition from the SD to HD minima (see Table I). Considering the fact that the ridges corresponding to the SD and HD minima are observed in neighboring nuclei, it is difficult to understand why the ridges corresponding to both minima have not been seen in the same nucleus.

The calculated kinematic and dynamic moments of inertia as well as transition quadrupole moments of the lowest HD solutions in the candidate HD nuclei are shown in Fig. 8. The calculated $J^{(2)}$ moments of inertia somewhat underestimate experimental data. The results of the MM calculations for ^{118}Te, ^{124}Xe, and ^{125}Cs (see Table I) are closer to experimental

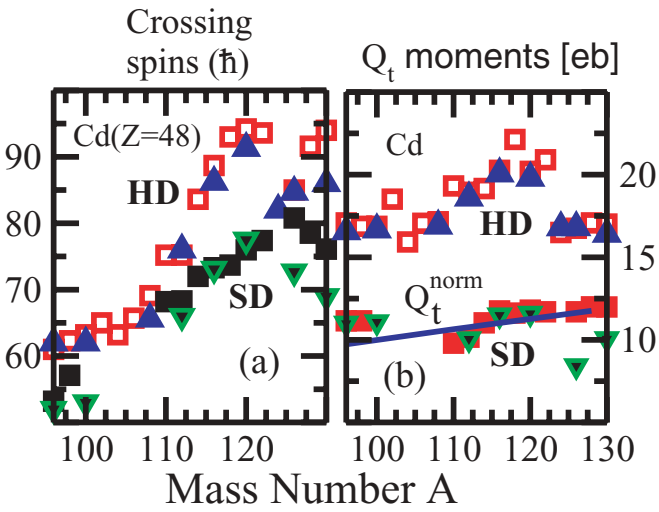

FIG. 6. (Color online) The same as in Fig. 4 but for the Cd isotopes. The results of the calculations with the NL1 (HD, open squares; SD, solid squares) and NL3 (HD, solid triangles up; SD, open triangles down) parametrizations of the RMF Lagrangian are presented. Note that the calculations with NL3 were performed only for selected nuclei.

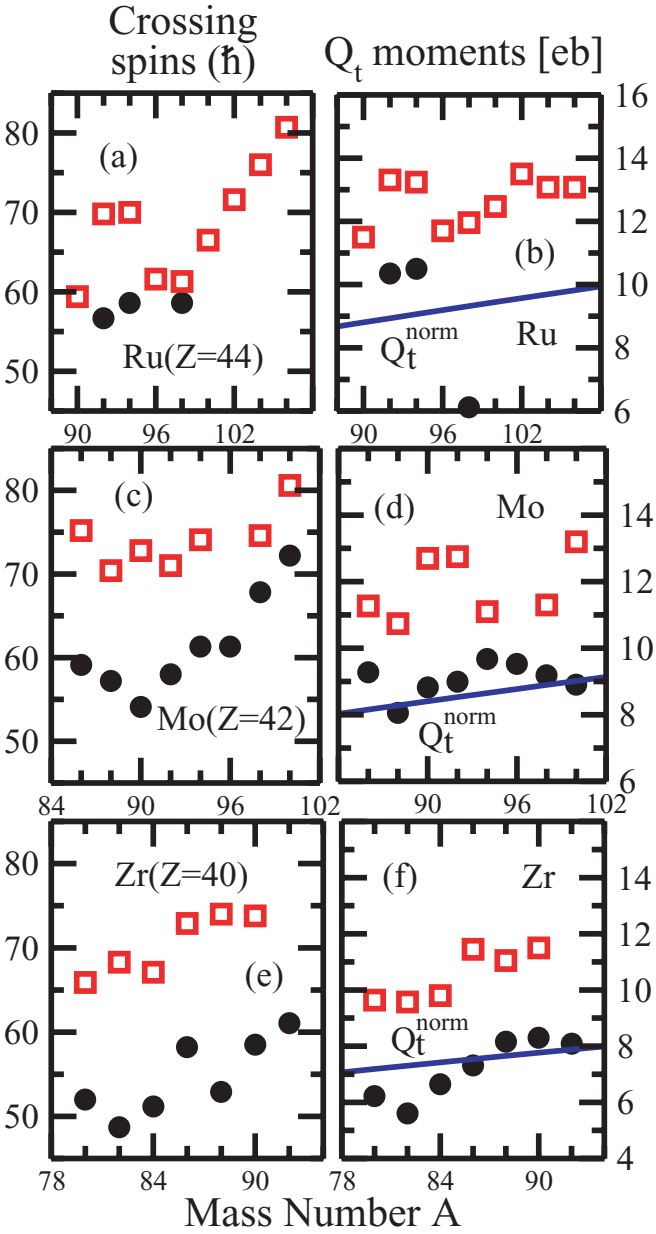

FIG. 7. (Color online) The same as in Fig. 4 but for the Ru, Mo, and Zr isotopes.

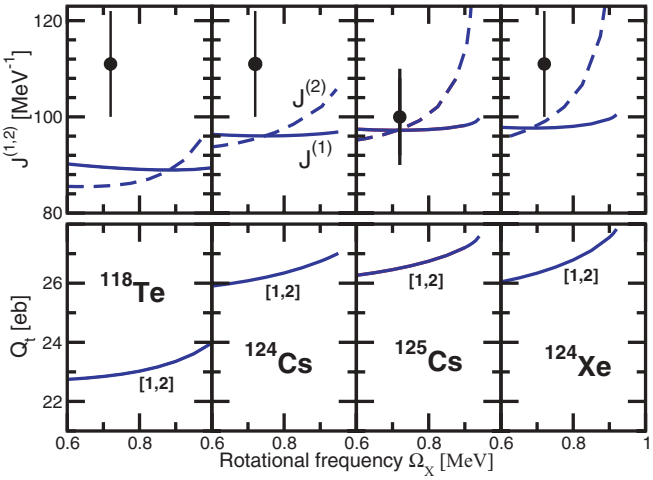

FIG. 8. (Color online) Calculated kinematic and dynamic moments of inertia (top panels) and transition quadrupole moments (bottom panels) as a function of rotational frequency for the lowest HD solutions in ^{118}Te, ^{124,125}Cs, and ^{124}Xe. The structure of calculated configurations is indicated at bottom panels. Experimental data for dynamic moments of inertia of ridge structures are shown in top panels.

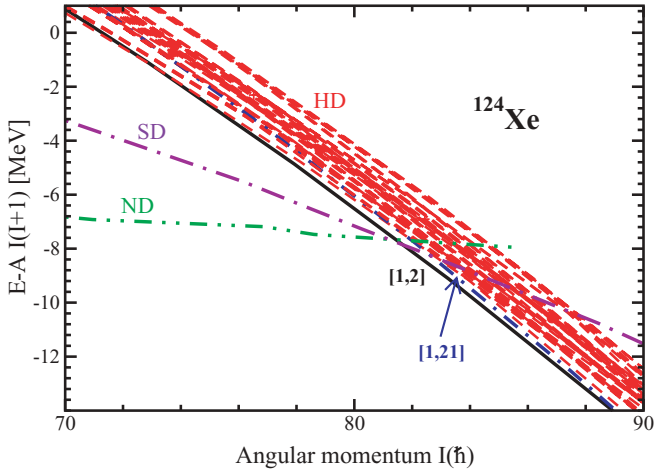

FIG. 9. (Color online) Energies of the calculated configurations relative to a smooth liquid drop reference $AI(I+1)$, with the inertia parameter $A = 0.01$. The ND and SD yrast lines are shown by dotted and dot-dot-dashed lines, respectively. Solid and dot-dashed lines are used for the [1,2] and [1,21] HD configurations, respectively. Dashed lines represent excited HD configurations.

data, but they are obtained at fixed quadrupole deformation β_2, whereas other deformation parameters β_4, β_6, and β_8 are automatically readjusted so as to minimize the total free Routhian for the vacuum configuration.

In the MM calculations, the kinematic moments of inertia of the configurations in the HD minimum decrease smoothly with the spin, whereas their dynamic moments of inertia are nearly constant (see Figs. 10 and 11 in Ref. [30]). The behavior of these observables as a function of rotational frequency (or spin) is completely different in the self-consistent CRMF calculations (see Figs. 8, 11, and Fig. 15 below). The kinematic moment of inertia is either nearly constant or very gradually increases with rotational frequency. The dynamic moment of inertia gradually increases over the calculated frequency range showing the features typical to the SD bands in the $A \sim 190$ mass region that are affected by pairing [3,67]: this is despite the fact that pairing is neglected in the CRMF calculations. The transition quadrupole moment Q_t is also increasing with rotational frequency; such a feature has not been seen before in the calculations without pairing for the SD bands. The microscopic origin of these unusual features will be discussed in more details in Sec. III C.

C. ^{124}Xe nucleus

The results of the CRMF calculations for some HD configurations in ^{124}Xe are displayed in Fig. 9. The HD minimum becomes lowest in energy at spin $82\hbar$, and the [1,2] configuration is the yrast HD configuration in the spin range of interest. The occupation of the single-particle orbitals in this configuration is presented in Fig. 10. The excited HD configurations displayed in Fig. 9 are built from this configuration by exciting either one proton or one neutron or simultaneously one proton and one neutron. The total number of excited HD configurations shown is 35. It interesting to mention that the configuration involving the lowest $N = 8$ neutron orbital (the [1,21] configuration in Fig. 9) is calculated at low excitation energy.

The calculations reveal a high density of the HD configurations that will be even higher if the additional calculations for the excited configurations would be performed starting from the low-lying excited HD configurations, such as the [1,21] configuration. This high density is due to two facts: relatively small $Z = 54$ and $N = 70$ HD shell gaps in the frequency range of interest (see Fig. 10) and the softness of the potential energy surfaces in the HD minimum. Figure 11(b) illustrates the latter feature: the particle-hole excitations discussed above, characterized by low excitation energy, lead to appreciable changes in the transition quadrupole moments Q_t. It is interesting to mention that there are large similarities between the single-particle Routhians in the vicinity of the $Z = 54$ and $N = 70$ HD shell gaps obtained in the CRMF calculations for yrast HD configuration in ^{124}Xe (Fig. 10) and the ones obtained in the Woods-Saxon calculations for the HD minimum in ^{122}Xe employing the so-called universal parametrization of the Woods-Saxon potential (see Figs. 8 and 9 in Ref. [30]). As a consequence, the high density of the excited HD states in ^{124}Xe is also expected in the MM calculations based on the formalism of Ref. [30].

The high density of the HD configurations may question our neglect of pairing. This is because there are numerous possibilities to scatter proton and neutron pairs and this process is energetically inexpensive due to the high density of the calculated configurations. To test the impact of pairing on the moments of inertia and binding energies, the comparative studies of the vacuum HD configuration and its unpaired analog in ^{124}Xe and of the vacuum SD configuration and its unpaired analog in ^{152}Dy have been performed within the cranked relativistic Hartree+Bogoliubov (CRHB) [68] and

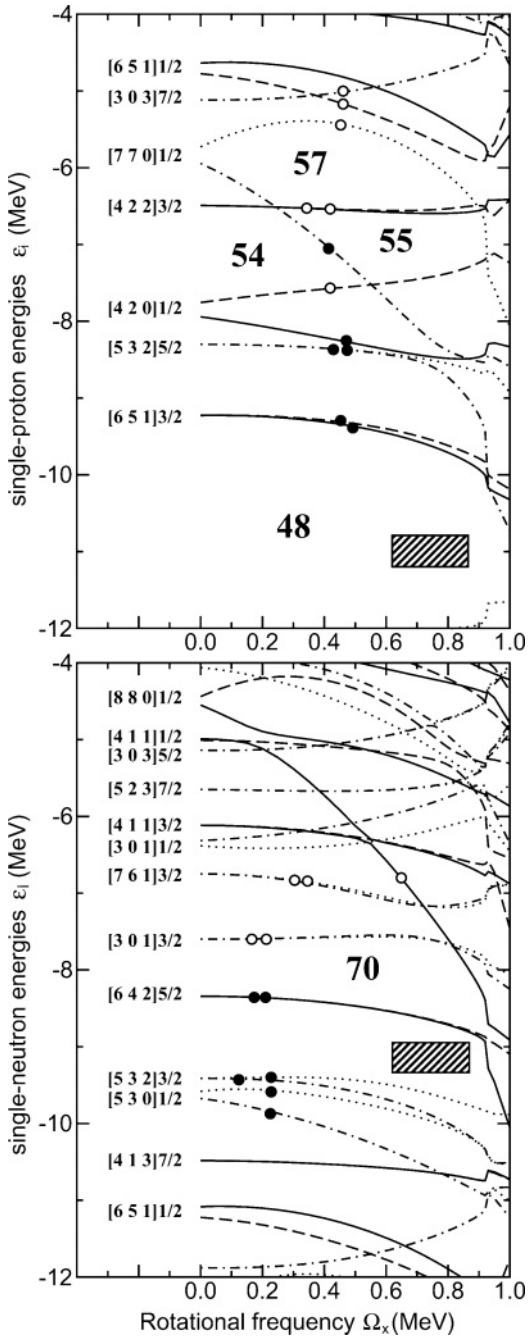

FIG. 10. Proton (top panel) and neutron (bottom panel) single-particle energies (Routhians) in the self-consistent rotating potential as a function of the rotational frequency Ω_x. They are given along the deformation path of the yrast HD configuration (the [1,2] conf. in Fig. 9) in ^{124}Xe and obtained in the calculations with the NL1 parametrization of the RMF Lagrangian. Long-dashed, solid, dot-dashed, and dotted lines indicate $(\pi = +, r = +i)$, $(\pi = +, r = -i)$, $(\pi = -, r = +i)$, and $(\pi = -, r = -i)$ orbitals, respectively. At $\Omega_x = 0.0$ MeV, the single-particle orbitals are labeled by the asymptotic quantum numbers $[Nn_z\Lambda]\Omega$ (Nilsson quantum numbers) of the dominant component of the wave function. Solid (open) circles indicate the orbitals occupied (emptied) in the [1,2] configuration. The dashed box indicates the frequency range corresponding to the spin-range $I = 60$–$85\hbar$ in this configuration.

CRMF approaches. An approximate particle number projection by means of the Lipkin-Nogami method is employed in the CRHB approach. Note that unpaired analog of the vacuum HD configuration in ^{124}Xe (built from the [1,2] configuration by the excitation of the proton from the $\pi[770]1/2(r = +i)$ orbital into the $\pi[420]1/2(r = +i)$ orbital, see Fig. 10) is nonyrast in the spin range of interest. As follows from this study, in both nuclei the pairing has a similar impact on the moments of inertia of the configurations under consideration. Taking into account that the SD bands in the $A \sim 150$ mass region are well described in the calculations without pairing [4,39], it is reasonable to expect that the neglect of pairing is a valid approximation for the moments of inertia of the HD bands in ^{124}Xe. Pairing leads to an additional binding of ~500 keV in the case of yrast SD band in ^{152}Dy; this additional binding slightly exceeds 1 MeV in the case of the vacuum HD configuration in ^{124}Xe. The dominant effects in the quenching of pairing correlations are the Coriolis antipairing effect and the quenching due to shell gaps: the latter effect being more pronounced in the SD bands of the $A \sim 150$ mass region because of the larger size of the SD shell gaps (see Fig. 4 in Ref. [4]). The third mechanism of the decrease of pairing is the blocking effect [69]. Due to this effect the impact of pairing on physical observables will be even lower in the HD bands of ^{124}Xe based on the excitation(s) of one (two) particles considered in Fig. 9. Thus, although weak pairing will somewhat modify the relative energies of different configurations, in no way will it create an energy gap between the vacuum and excited configurations.

The calculations suggest that it will be difficult to observe discrete HD bands in ^{124}Xe because their high density will lead to a situation in which the feeding intensity will be redistributed among many low-lying bands, thus drastically reducing the intensity with which each individual band is populated. However, the high density of the HD bands may favor the observation of the rotational patterns in the form of ridge-structures in three-dimensional rotational mapped spectra as it has been seen in the HLHD experiment [31].

Figure 8 shows that the HD shapes undergo a centrifugal stretching that result in an increase of the transition quadrupole moments Q_t with increasing rotational frequency. This process also reveals itself in the moments of inertia: the kinematic moments of inertia are either nearly constant or slightly increase with increasing rotational frequency, whereas the dynamic moments of inertia increase continuously and substantially over the frequency region of interest. On the contrary, the dynamic moments of inertia of the HD bands are almost constant as a function of rotational frequency in the MM calculations (see Figs. 10 and 20 in Ref. [30]), which is most likely a consequence of fixed quadrupole deformation. The above-mentioned features are general ones for the HD bands in the $A \sim 120$ mass region, see Figs. 8, 11, and 15. They are in complete contract to the features of the SD bands in unpaired regime, in which the Q_t, $J^{(1)}$, and $J^{(2)}$ values (apart from the unpaired band crossing regions) decrease with increasing rotational frequency (see Refs. [4,37,44,49] and references therein).

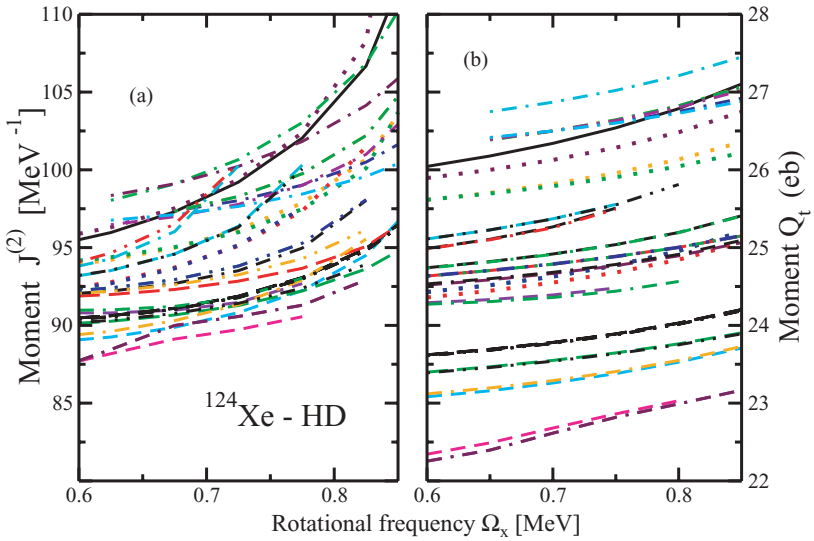

FIG. 11. (Color online) Dynamic moments of inertia $J^{(2)}$ (panel a) and transition quadrupole moments Q_t (panel b) of the HD configurations in ^{124}Xe shown in Fig. 9. They are displayed as a function of rotational frequency Ω_x. The regions of band crossings are excluded in these plots.

Systematic analysis of the yrast/near-yrast HD configurations in the part of the nuclear chart under investigation shows that the centrifugal stretching is a general feature. At the spins, where the HD minimum is lowest in energy, it reveals itself (with very few exceptions) by the increase of transition quadrupole Q_t and mass hexadecapole Q_{40} moments. Only in a few HD bands, characterized by the modest transition quadrupole moment, at low rotational frequencies these quantities decrease with increasing Ω_x. However, even in these bands the Q_t and Q_{40} values start to increase above specific value of rotational frequency. Similar features are also seen in the dynamic moments of inertia; with a few exceptions the $J^{(2)}$ values increase in the spin range of interest. The variations (both the increases and decreases) in the kinematic moments of inertia are rather small ($\sim$2% of absolute value) in the frequency range of interest.

The basis of the CRMF model is sufficiently large to see if there is a tendency for the development of necking. Figure 12 shows some indications of the necking and the clusterization of the density into two fragments in the [1,2] configuration of ^{124}Xe, but this effect is not very pronounced in this nucleus.

The kinematic and dynamic moments of inertia as well as the transition quadrupole and mass hexadecapole moments of the [1,2] configuration in ^{124}Xe are shown for different parametrizations of the RMF Lagrangian in Fig. 13. The gradual increase of all physical observables is due to centrifugal stretching. The NLZ (NLSH) parametrizations provide the largest (smallest) values of the above mentioned physical observables, whereas the results obtained with NL1 and NL3 are in between those results. Similar relations between the results obtained with these parametrizations also exist in other regions of nuclear chart studied so far in the CRMF or CRHB frameworks, namely in the $A \sim 60$ [70], $A \sim 150$ [39], and $A \sim 190$ [68] regions of superdeformation and in the $A \sim 250$ [51] region of normal deformation. The NL1 and NL3 parametrizations, which have been extensively used in the previous studies of rotating systems and superdeformation [44], give the values of physical observables of interest which differ only by few percentages. It is known that the NLSH parametrization somewhat underestimates the experimental moments of inertia [39,70]. The NLZ parametrization has not been used in the previous studies of rotating systems, so it is unknown how well it describes such systems.

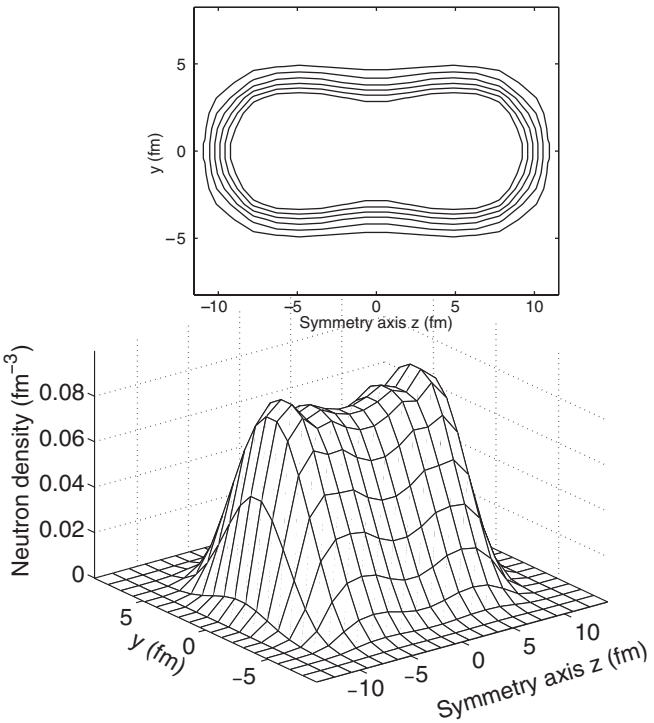

FIG. 12. The self-consistent neutron density $\rho_n(y, z)$ as a function of y and z coordinates for the [1,2] configuration in ^{124}Xe at rotational frequency $\Omega_x = 0.75$ MeV. Top and bottom panels show two- and three-dimensional plots of the density distribution, respectively. In the top panel, the densities are shown in steps of 0.01 fm^{-3} starting from $\rho_n(y, z) = 0.01$ fm^{-3}.

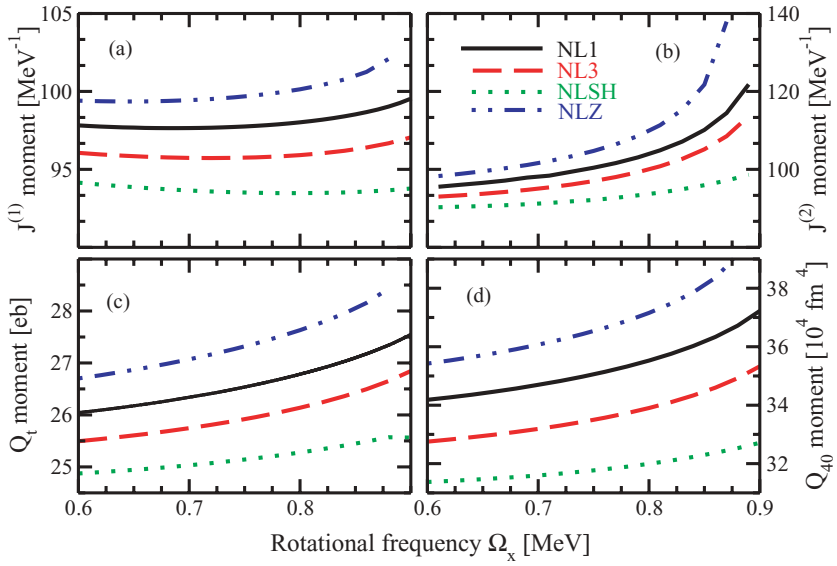

FIG. 13. (Color online) Kinematic [$J^{(1)}$] and dynamic [$J^{(2)}$] moments of inertia as well as transition quadrupole Q_t and mass hexadecupole Q_{40} moments of the [1,2] configuration in ^{124}Xe calculated with different parametrizations of the RMF Lagrangian.

D. Single-particle properties at hyperdeformation: an example of neighborhood of ^{124}Xe.

The role of the single-particle degrees of freedom at hyperdeformation was mainly overlooked in the previous studies. It has been studied to some extent only within the MM method in Refs. [10,30]. However, the studies of Ref. [30] suggest that the ^{124}Xe nucleus is very rigid in the HD minimum: the dynamic moments of inertia of different HD bands differ by no more than 2%, and their changes as a function of spin are very small (see Fig. 10 in Ref. [30]). Similar results were obtained for HD bands in ^{146}Gd and ^{152}Dy in Ref. [10].

On the contrary, the CRMF calculations for the dynamic moment of inertia of the yrast and excited HD configurations in ^{124}Xe show much larger spread and much larger variations as a function of rotational frequency; see Fig. 11(a). In addition, large variations in the calculated transition quadrupole moments Q_t of these configurations are clearly seen in Fig. 11(b). This suggests that the HD minimum is relatively soft and that the individual properties of the single-particle orbitals play an important role in the definition of the properties of the HD bands. One of our goals is to investigate the impact of the particle in a specific single-particle orbital on the properties of the HD bands and to study whether the methods of configuration assignment based on the relative properties of different bands are also applicable at HD.

1. *The structure of the wave function*

The structure of the wave function at HD is analyzed on the example of a few single-particle orbitals of the [1,2] configuration in ^{124}Xe (Fig. 14). The evolution of these orbitals in energy with rotational frequency is displayed in Fig. 10. The

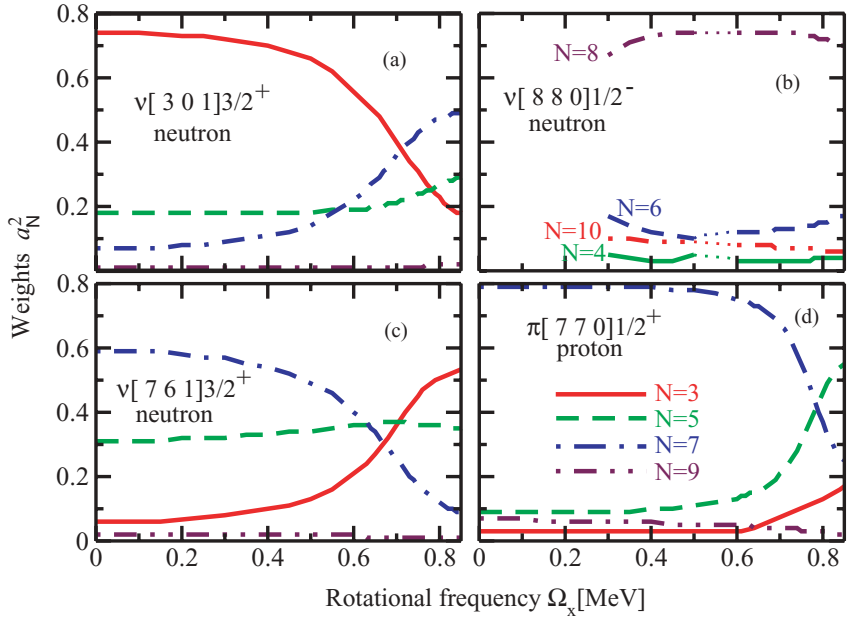

FIG. 14. (Color online) The weights a_N^2 of different N components in the structure of the wave functions of the indicated orbitals. They are shown as a function of rotational frequency. For simplicity, the region of the crossing between the $\nu[880]1/2^-$ and $\nu[411]3/2^-$ orbitals at $\Omega_x \sim 0.55$ MeV is removed; dotted lines are used in panel (b) to connect the weights corresponding to the $\nu[880]1/2^-$ orbital before and after crossing.

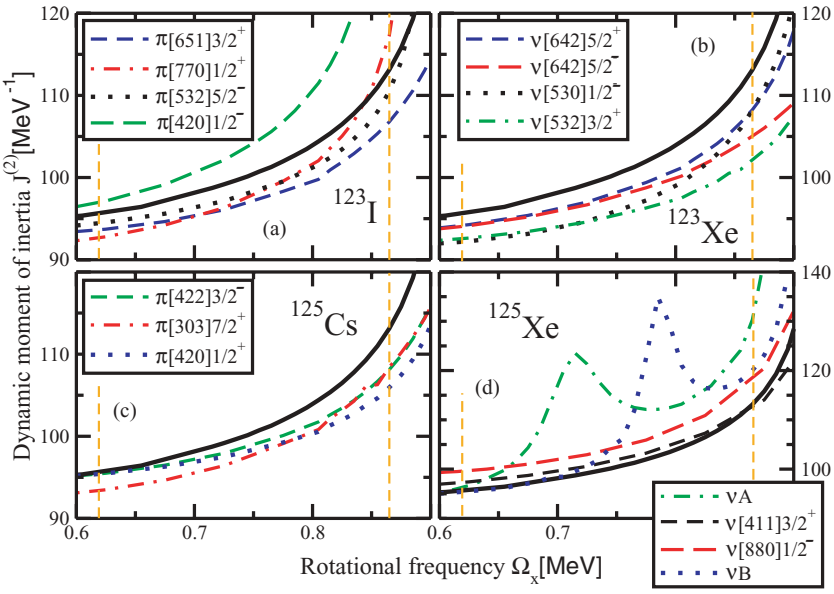

FIG. 15. (Color online) Dynamic moments of inertia $J^{(2)}$ of selected configurations in ^{124}Xe and neighboring nuclei. Dynamic moment of inertia of the [1,2] configuration A in ^{124}Xe is shown by a thick solid line in each panel. The $J^{(2)}$ values of the configurations in the nucleus indicated on the panel are displayed by the lines of other types. These configurations differ from the [1,2] configuration A in ^{124}Xe in the occupation of the orbitals shown in the panels. Vertical dashed lines indicate the frequency range corresponding to the spin range $I = 60$–$85\hbar$ in the [1,2] configuration of ^{124}Xe.

wave function Ψ is expanded into the basis states by

$$\Psi = \sum_{N,\alpha} c_{N,\alpha} |N\alpha\rangle, \tag{9}$$

where N and α represent the principal quantum number and the set of additional quantum numbers specifying the basis state, respectively. We specify the weight a_N^2 of the basis states belonging to the specific value of N in the structure of the wave function as

$$a_N^2 = \sum_{N-\text{fixed},\alpha} c_{N,\alpha}^2 \tag{10}$$

with the condition $\sum_N a_N^2 = 1$ following from the orthonormalization of the wave function of the single-particle orbital.

Hyperdeformation leads to a considerable fragmentation of the wave function over N, which is much larger than in the case of SD. In the regions away from the band crossing the weight a_N^2 of the dominant N component of the wave function does not exceed 0.8, whereas the weight of second largest component is typically around 0.2 (Fig. 14). Very strong fragmentation of the wave function is seen in the case of the $\nu[761]3/2^+$ orbital: before the band crossing the weights of the $N = 7$ and $N = 5$ components of the wave function are approximately 0.6 and 0.3, respectively. Even stronger fragmentation is seen in the region of the band crossing of the $\nu[761]3/2^+$ and $\nu[301]3/2^+$ orbitals at $\Omega_x \sim 0.7$ MeV (Figs. 10) where they strongly interact and gradually exchange their character [Figs. 14(a) and 14(c)]. Similar fragmentation is also seen for the $\pi[770]1/2^+$ orbital (Fig. 14) that interacts strongly with the $\pi[532]5/2^+$ orbital in the band crossing region at $\Omega_x \sim 0.8$ MeV (Fig. 10).

2. *The methods of configuration assignment*

The HD bands in nuclei neighboring to ^{124}Xe, which differ by either one proton or one neutron from the [1,2] configuration in ^{124}Xe, and their relative properties with respect of the [1,2] configuration in ^{124}Xe, are studied to investigate the applicability of different methods of configuration assignment at HD.

The dynamic moments of inertia for the four HD bands in each of these nuclei are compared with the one of the [1,2] configuration in ^{124}Xe in Fig. 15. The difference between the dynamic moments of inertia of the configurations in nuclei with masses A and $A \pm 1$ is due to the impact of the particle in the specific single-particle orbital by which two compared configurations differ. The results of the calculations question conventional wisdom [37] that the largest impact on the dynamic moment of inertia is coming from the particles in the intruder orbitals. Indeed, the impact of the neutron in the hyperintruder $\nu[880]1/2^-$ orbital on the dynamic moments of inertia [Fig. 15(d)] is comparable to the one of nonintruder $\nu[642]5/2^+$ orbital or even smaller by a factor of $\sim$2 than the impact due to the neutron in nonintruder $\nu[532]3/2^+$ orbital [Fig. 15(b)]. A similar situation is also seen for protons, where, for example, the impact of the proton in the hyperintruder $\pi[770]1/2^+$ orbital is smaller than its impact in the nonintruder $\pi[420]1/2^-$ orbital. This suggests that not only angular momentum, carried by the particle in specific single-particle orbital, but also polarization effects it induces into time-even and time-odd mean fields [52] are important when considering relative properties of two configurations. Based on this example, one can conclude that the configuration assignment of the HD bands, based only on the relative properties of the dynamic moments of inertia of two compared bands, is unreliable.

The configuration assignments at SD have been mostly based on the effective alignment approach (see Refs. [38, 39,70] and references therein). The success of this method is due to the fact that it was possible to separate intruder and nonintruder orbitals because the former show pronounced dependence of the effective alignments i_{eff} on the rotational frequency (see, for example, Figs. 2, 3, 5, 6, and 8 in Ref. [39]). On the contrary, the effective alignments of nonintruder orbitals are typically constant as a function of

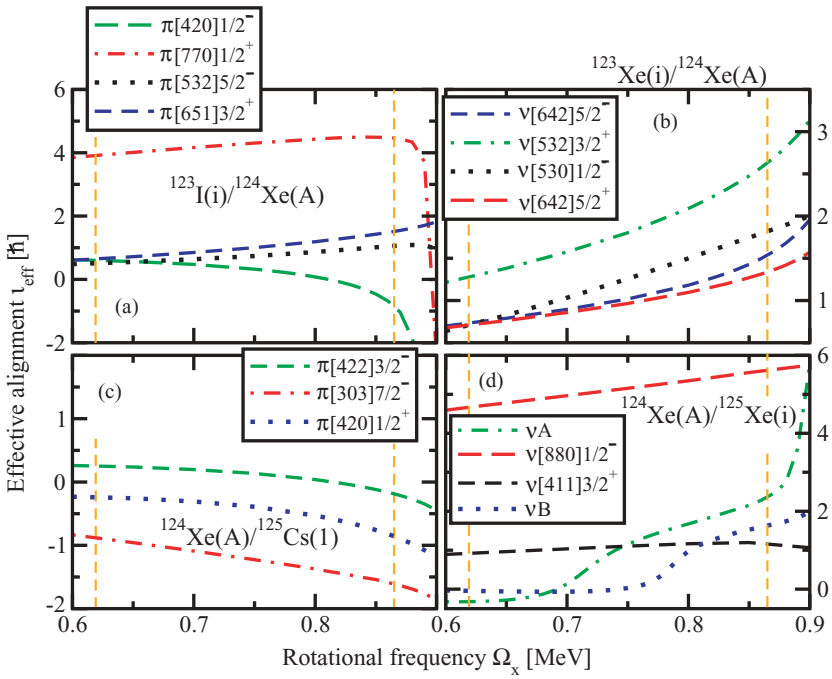

FIG. 16. (Color online) Effective alignments $i_{\rm eff}$ extracted from the calculated configurations for the orbitals active in the vicinity of the $Z = 54/55$ and $N = 70$ HD shell gaps (see Fig. 10). The calculated configurations are the [1,2] configuration in ^{124}Xe and the configurations in neighboring nuclei (shown in Fig. 15) obtained by adding or removing a single particle (proton or neutron). The effective alignment between configurations X and Y is indicated as "X/Y." The configuration X in the lighter nucleus is taken as a reference, so the effective alignment measures the effect of the additional particle. The compared configurations differ in the occupation of the orbitals shown in the panels. Note that the vertical scale of different panels is different. Vertical dashed lines indicate the frequency range corresponding to the spin range $I = 60$–$85\hbar$ in the configuration A of ^{124}Xe.

rotational frequency. It also follows from the studies in the $A \sim 140$–150 region of superdeformation that the change of effective alignment by $\approx 1\hbar$ within the observed frequency range allows us to identify aligning intruder orbitals with a high level of confidence.

A configuration assignment based on the effective alignments depends on how accurately these alignments can be predicted. For example, the application of the effective alignment approach in the $A \sim 140$–150 region of superdeformation requires an accuracy in the prediction of $i_{\rm eff}$ on the level of $\sim 0.3\hbar$ and $\sim 0.5\hbar$ for nonintruder and intruder orbitals, respectively [3,38,39]. In the highly deformed and SD bands from the $A \sim 60$–80 mass region, these requirements for accuracy are somewhat relaxed [48,70]. We expect that in the $A \sim 125$ mass region of HD, the effective alignments should be predicted with a precision similar to that in the $A \sim 140$–150 region for a reliable configuration assignment.

Our analysis shows that a reliable configuration assignment for the HD bands based solely on the effective alignment approach will be problematic (at least in the $A \sim 125$ mass region) because of several reasons. First, the hyperintruder orbitals do not show appreciable variations of $i_{\rm eff}$ with rotational frequency. Figure 16 shows that the effective alignments of the hyperintruder orbitals such as $\pi[770]1/2^+$ and $\nu[880]1/2^-$ show little variations with rotational frequency [see Figs. 16(a) and 16(d)]. On the contrary, the effective alignments of the $\nu[532]3/2^+$ and $\nu[530]1/2^-$ orbitals show much larger variations reaching $1.5\hbar$ in the spin range $I = 60$–$85\hbar$ in the case of the latter orbital [see Fig. 16(b)]. However, the variations of $i_{\rm eff}$ as a function of rotational frequency are small for the majority of the orbitals in the spin range of interest. Thus, contrary to the case of SD, it will be more difficult to distinguish among hyperintruder, intruder, and nonintruder orbitals based on the variations of $i_{\rm eff}$ with rotational frequency. This situation will become even more complicated if the suggestion of Ref. [30] that the spin range over which the HD bands are expected to be observed ($24\hbar$ at the most; this is shorter than in the case of SD) is true. These two features [small variations of $i_{\rm eff}$ and expected spin (frequency) range of the HD bands] will lead to a situation where the $i_{\rm eff}$ values for many orbitals will look alike within the typical "error bars" of the description of $i_{\rm eff}$ by theoretical models, so that it will be difficult to distinguish between them within the framework of the effective alignment approach.

Similar to the case of SD [40,41], additional information on how the single particle affects the properties of the HD bands can be extracted from the relative transition quadrupole moments ΔQ_t. Figure 17 shows that the hyperintruder $\pi[770]1/2^+$ and $\nu[880]1/2^-$ orbitals with $\Delta Q_t \approx 2$ eb and $\Delta Q_t \approx 1.25$ eb have the largest impact on the transition quadrupole moments among the studied proton and neutron orbitals. One has to keep in mind that the addition of a proton changes the proton number by 1. This change contributes approximately 0.5 eb in relative transition quadrupole moment ΔQ_t of the proton orbitals. This effect is not present in the ΔQ_t values of the neutron orbitals.

The ΔQ_t values were used only as a complimentary tool of the configuration assignment at SD. This is because of the difficulty to measure them in experiment [71,72] and the fact that they show little variation as a function of rotational frequency, thus providing less information than $i_{\rm eff}$. The same features are also valid at HD; see Fig. 17 for the variations of the ΔQ_t values. In addition, some single-particle orbitals such as $\pi[422]3/2^-$ and $\pi[303]7/2^-$ [Fig. 17(c)] show very similar ΔQ_t values. This will not allow us to make a unique

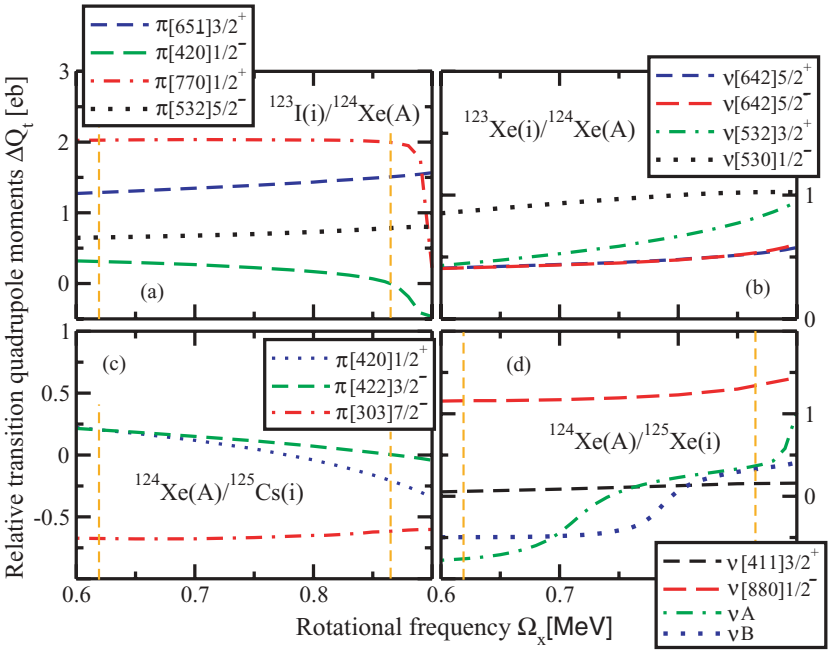

FIG. 17. (Color online) Relative transition quadrupole moments $\Delta Q_t = Q_t(A+1) - Q_t(A)$ (A is the mass of the nucleus) extracted from the calculated configurations in indicated nuclei. The compared configurations are shown as "X/Y": the configuration X in the lighter nucleus is taken as a reference, so the ΔQ_t measures the effect of the additional particle placed in the orbitals shown in the panels. Vertical dashed lines indicate the frequency range corresponding to the spin range $I = 60$–$85\hbar$ in the [1,2] configuration of ^{124}Xe.

configuration assignment even if the experimental ΔQ_t values for these orbitals are available. However, their $i_{\rm eff}$ values differ by $\sim 1\hbar$ [Fig. 16(c)], and this fact can be used in the configuration assignment.

However, the fact that in general the effective alignment approach fails to provide a unique configuration assignment at HD increases the role of the method of configuration assignment based on relative transition quadrupole moments. Our analysis shows that *only simultaneous application of these two methods by comparing experimental and theoretical* ($i_{\rm eff}$, ΔQ_t) *values will lead to a reliable configuration assignment at HD*.

Let us illustrate this on the hypothetical example of two "experimental" bands; one in ^{123}I and another in ^{124}Xe. In this example, the [1,2] configuration is assigned to the band in ^{124}Xe. Let us assume that the effective alignments in the ^{123}I/^{124}Xe pair of the bands increase from $4.0\hbar$ to $4.25\hbar$ in the frequency range 0.62–0.87 MeV under selected spins of these bands. Under these conditions, the "experimental" bands differ in the occupation of the $\pi[770]1/2^+$ orbital [Fig. 16(a)]. However, it is reasonable to expect that the spins of "experimental" bands will not be fixed, so these changes in effective alignment should be from $(4.0+n)\hbar$ to $(4.25+n)\hbar$, where $n = 0, \pm 1, \pm 2, \ldots$. Assuming that the accuracy of the description of effective alignments in theoretical calculations is around $0.4\hbar$, one can conclude that for $n = -3$ the "experimental" bands can also differ in the occupation of either the $\pi[532]5/2^-$ or $\pi[651]3/2^+$ orbitals [Fig. 16(a)]. In a similar way to the $A \sim 150$ region of SD [38,39], the systematic studies of the pairs of the bands that differ by one proton may narrow the choice of the orbitals involved. However, the ΔQ_t values for these orbitals are drastically different; $\Delta Q_t \approx 2.0$ eb for the $\pi[770]1/2^+$ orbital, $\Delta Q_t \approx 1.4$ eb for $\pi[651]3/2^+$, and $\Delta Q_t \approx 0.7$ eb for $\pi[532]5/2^-$ (see Fig. 17). So, if both quantities, $i_{\rm eff}$ and ΔQ_t, are measured simultaneously, a unique configuration assignment for "experimental" band in ^{123}I will be possible.

The band crossing features of the HD bands provide an additional tool of configuration assignment that can be used more frequently than in the case of the SD bands because of strong mixing between the different N shells at HD. The large peaks in $J^{(2)}$ of the νA and νB configurations in ^{125}Xe [Fig. 15(d)] are due to the band crossings with a strong interaction. These crossings are also visible in the effective alignments $i_{\rm eff}$ [Fig. 16(d)] and relative transition quadrupole moments ΔQ_t [Fig. 17(d)]. They originate from the crossing of the same signatures of the $\nu[301]3/2$ and $\nu[761]3/2$ orbitals, where νA and νB have signatures $r = +i$ and $r = -i$, respectively. The former orbital is occupied before band crossing, the latter after band crossing. An unusual feature of these band crossings is the fact that they originate from the interaction of the orbitals, the dominant N components of which differ by $\Delta N = 4$. At SD, the crossings between the orbitals dominated by different N shells have been characterized by a weak interaction leading to a sharp jump in $J^{(2)}$ [4,73,74]. The observed unpaired SD band crossings with strong interaction are between the orbitals with the same dominant N shells and they were observed in the nuclei around ^{147}Gd [4,75].

E. General observations: the density of the HD bands and the necking degree of freedom

As discussed in Sec. III C on the example of ^{124}Xe, the high density of the HD bands is one of the major obstacles for the observation of discrete HD bands. It will lead to a situation where the feeding intensity will be redistributed among many low-lying HD bands, thus drastically reducing the intensity with which each individual band is populated. As a consequence, the feeding intensity of an individual HD band will drop below the observational limit of experimental

facility; this fact has to be taken into account when planning future experiments for a search of discrete HD bands.

Two factors contribute to the high density of the HD bands, namely relatively small proton and neutron HD shell gaps in the frequency range of interest and the softness of the potential energy surfaces in the HD minimum (see Sec. III C). Systematic mapping of the density of the HD states as a function of the proton and neutron numbers is too costly in the computational sense because it involves the calculation of the lowest in energy particle-hole excitations. Thus, we decided to look at the problem of the density of the HD states in a somewhat simplistic way by considering the proton and neutron energy gaps between the last occupied and the first unoccupied states in the yrast HD configurations; the small size of these gaps will most likely point to the high density of the HD bands.

The analysis of the Nilsson diagrams in Fig. 18 already reveals some HD gaps in the single-particle spectra. At the values of $Q_0 \sim 17$–20 eb typical for the HD configurations in Cd isotopes [Fig. 6(b)], there are very large proton $Z = 48$ and neutron $N = 48$ HD shell gaps and smaller neutron gaps at $N = 58$ and 60. In general, this figure suggests that the hyperdeformation will be more favored in the nuclei with a similar number of protons and neutrons because the proton and neutron shell effects for the HD shapes will act coherently; this trend has already been seen in the crossings spins $I_{\rm cr}^{\rm HD}$ for different isotope chains in Sec. III A.

The size of these gaps and their presence will be altered (especially for medium- and small-size energy gaps) when the rotation and the self-consistent readjustment of the neutron and proton densities with the change of particle number are taken into account. Indeed, this is seen in Fig. 19, which shows the energy gaps between the last occupied and first unoccupied single-particle orbitals as a function of the neutron number for different isotope chains. The largest proton gap at $Z = 48$ is seen in Cd isotopes; its size is around 1.5 MeV in proton-rich nuclei and it increases up to 3 MeV with the increase of neutron number. In other isotope chains, the size of the proton energy gap is smaller than in Cd isotopes and it fluctuates around 1 MeV. For the majority of the nuclei, the size of the neutron energy gap fluctuates around 1 MeV. However, its size increases up to 1.5 MeV in some nuclei and in ^{96}Cd it reaches 2 MeV (see Fig. 19 for details).

Taking into account that the proton and neutron HD shell gaps in ^{124}Xe are around 1 MeV (Fig. 10) and considering the results for the density of the HD states in this nucleus as a reference (Sec. III C), one can conclude that the analysis of the energy gaps suggests that in most of the nuclei the density of

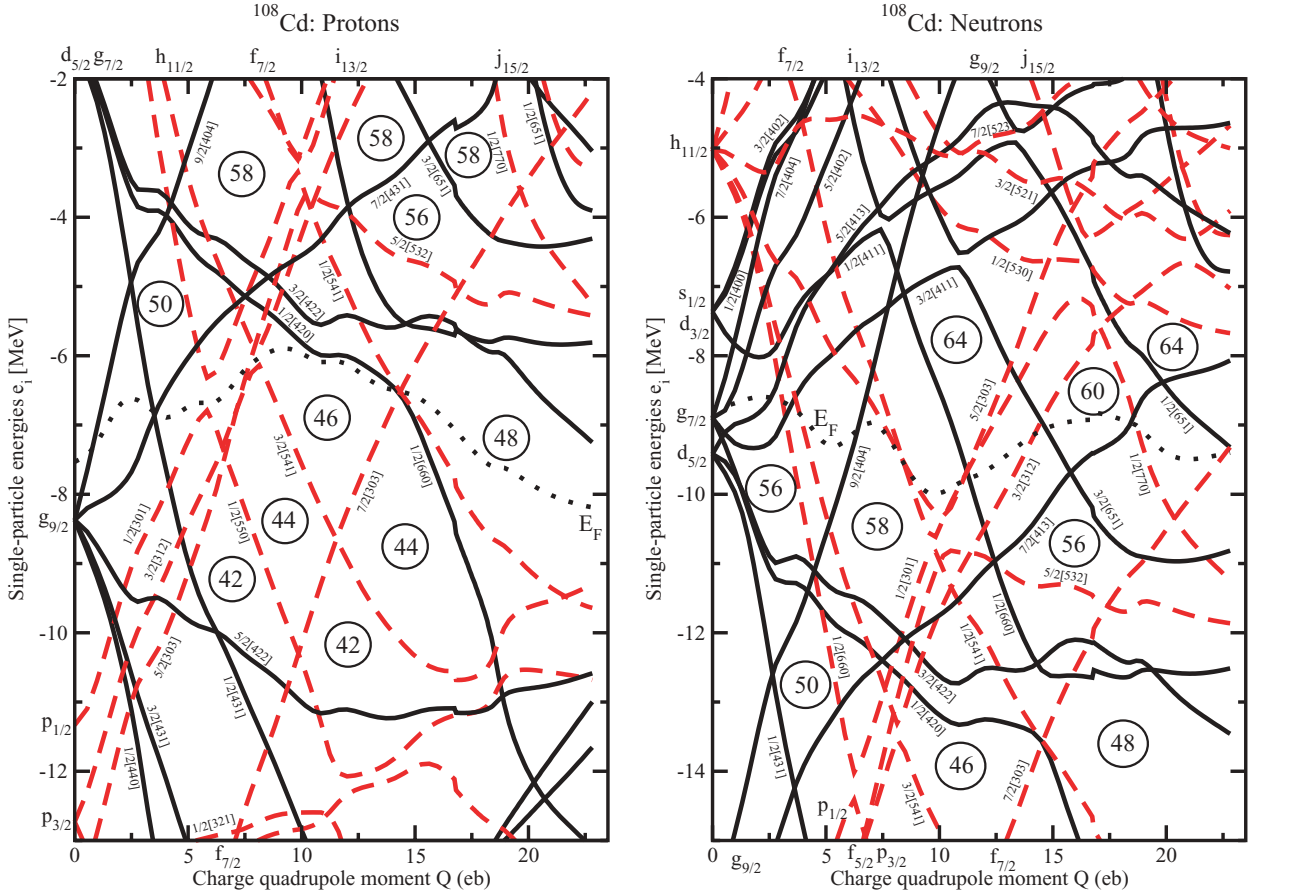

FIG. 18. (Color online) Proton and neutron single-particle energies in ^{108}Cd as a function of charge quadrupole moment Q, obtained in the axially symmetric RMF calculations. Solid and dashed lines denote positive- and negative-parity orbitals, respectively. The Fermi energy E_F is shown by dotted line. The single-particle orbitals are labeled by the Nilsson quantum numbers. Large shell gaps are indicated.

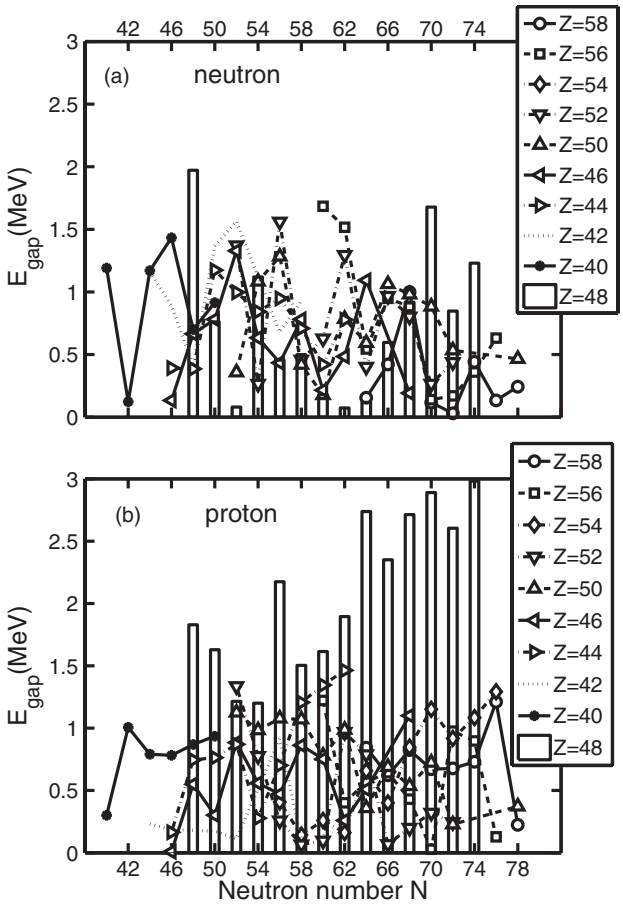

FIG. 19. The energy gaps between the last occupied and first unoccupied single-particle orbitals shown as a function of neutron number for different isotope chains. They are extracted from the Routhian diagrams of the lowest HD configurations at the spin values where these configurations become yrast. The bars are used for the energy gaps in the Cd isotopes.

the HD bands will be high. For these nuclei, the observation of discrete HD bands using existing facilities is most likely not possible. The only exceptions are Cd nuclei and a few nuclei in which the size of at least one gap reaches 1.5 MeV (see Fig. 19 for details). For example, in Cd nuclei the large size of the $Z = 48$ HD shell gap (especially, for nuclei in the valley of the β stability) will make proton particle-hole excitations energetically expensive. As a consequence, the density of the HD bands has to be lower in Cd isotopes as compared with the one in other isotopes.

One has to remember that the high density of the HD bands is not necessarily a negative factor. It favors the observation of the rotational patterns in the form of ridge structures in three-dimensional rotational mapped spectra as it has been seen in the HLHD experiment for a few nuclei [31]. The observation of ridge structures as a function of proton and neutron number, which seems to be feasible with existing experimental facilities such as GAMMASPHERE, will provide invaluable information about HD at high spin.

The importance of the necking degree of freedom for the high-spin HD states has been studied in the MM approach in Refs. [8,15]. However, this degree of freedom has not been investigated in detail at high spin in self-consistent approaches so far. To fill this gap in our knowledge, the systematics of the self-consistent proton density distributions in the HD states obtained in the CRMF calculations are shown in Fig. 20. One can see that in some nuclei such as ^{124}Te, ^{130}Xe, ^{132}Ba the necking degree of freedom plays an important role, whereas others (for example, ^{100}Mo and ^{136}Ce) show no necking. The neck is typically less pronounced in the HD states of the lighter nuclei because of their smaller deformation (see also Fig. 5 in Ref. [20]). It becomes even more important in extremely deformed structures that according to the language of Ref. [5] can be described as megadeformed. Figure 21 shows an example of density distribution for the megadeformed state in ^{102}Pd, which becomes yrast at $I \sim 85\hbar$ in the CRMF calculations. The neck is more pronounced in the proton subsystem than in the neutron one both in the HD and megadeformed structures due to the Coulomb repulsion of the segments. This is illustrated in Fig. 21. Our self-consistent calculations indicate that the shell structure is also playing a role in a formation of neck. For example, the neck is visible in ^{132}Ba but is not seen in ^{116}Ba (Fig. 20). This is contrary to the fact that the calculated transition quadrupole moments of the HD states in these nuclei [Fig. 4(d)] and their density elongations (Fig. 20) are comparable. These results indicate that, in general, the necking degree of freedom is important in the HD states and that it should be treated within the self-consistent approach that, in particular, allows different necking for the proton and neutron subsystems.

IV. ^{111}I NUCLEUS: A CANDIDATE FOR A DOUBLY MAGIC EXTREMELY SD BAND

The results of the CRMF calculations for the configurations forming the yrast line or located close to it in energy are shown in Fig. 22. According to the calculations, normal- and highly deformed bands, many of which show the high triaxiality that is indicative of approaching band termination [55], dominate the yrast line up to $I \approx 64\hbar$. At higher spin, more deformed structures become yrast. The configuration A has the structure $\pi 6^1 \nu 6^2$ and is yrast in the spin range $I = 64$–$73\hbar$: no hyperintruder $N = 7$ orbitals are involved in its structure. In this spin range it is characterized by the transition quadrupole moment $Q_t \sim 15.7\ eb$ and by the γ deformation of $\sim 1^\circ$. The normalized transition quadrupole moment in this system is $Q_t^{\rm norm} = 11.7\ eb$, thus this band is approximately 35% more deformed than the SD band in ^{152}Dy. As a consequence, in terms of deformation, this band can be characterized as an extremely superdeformed (ESD) band that is only slightly less deformed than the HD bands.

In addition, the configuration A is well separated from the excited SD/HD configurations below $I \sim 73\hbar$ (see Fig. 22). This is due to the presence of the large $Z = 53$ and $N = 58$ ESD shell gaps in the single-particle spectra (see Fig. 23). In this configuration, all single-particle states below the $Z = 53$ and $N = 58$ ESD shell gaps are occupied by protons and neutrons, respectively. Thus, this ESD band is a doubly magic

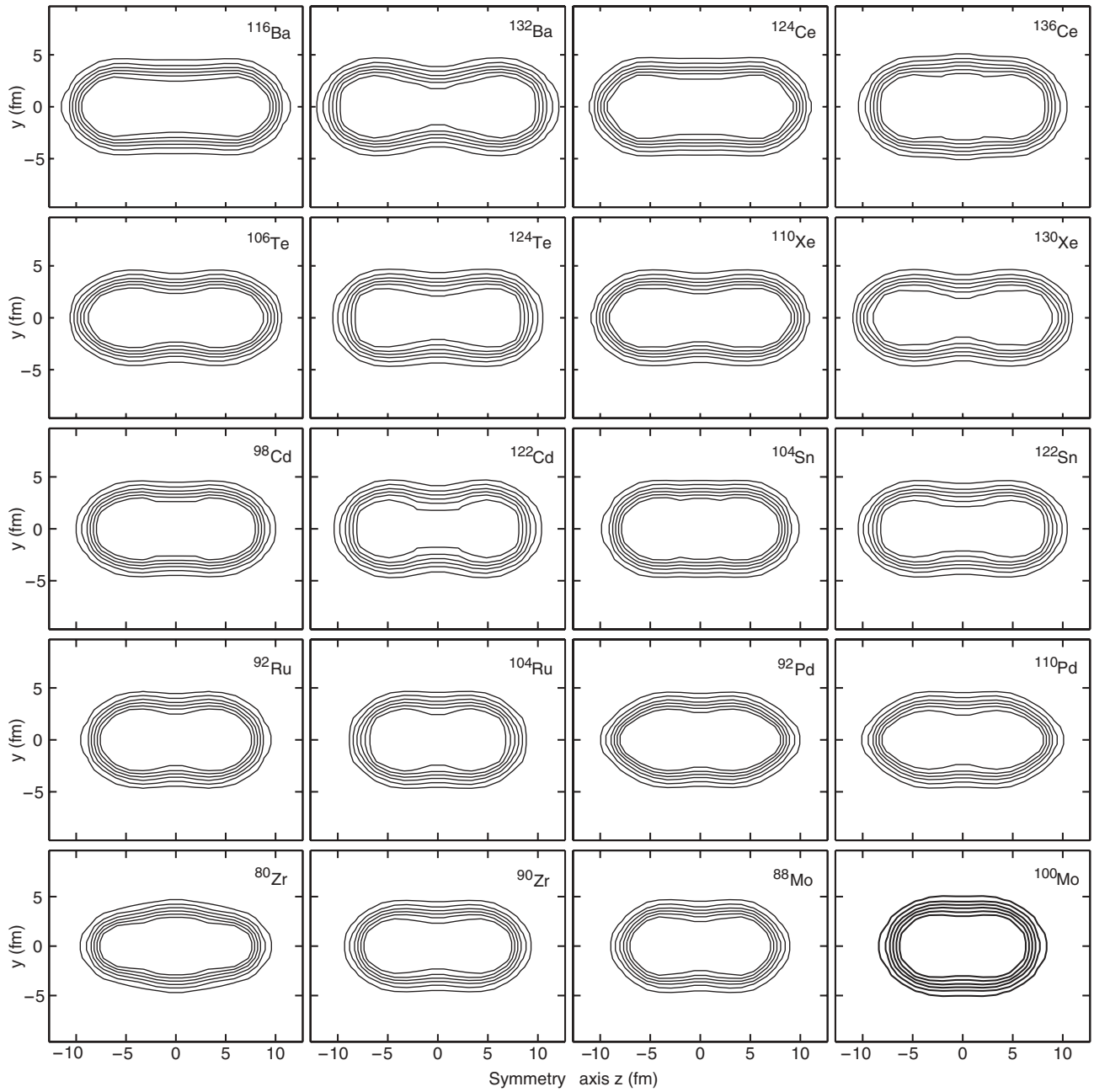

FIG. 20. The self-consistent proton density $\rho_p(y, z)$ as a function of y and z coordinates for the HD configurations. They are displayed at spin values at which these configurations become yrast. For each isotope chain, the densities in two nuclei (typically, most proton- and neutron-rich ones included in calculations) are shown. The densities are displayed in steps of 0.01 fm^{-3} starting from $\rho_p(y, z) =$ 0.01 fm^{-3}.

one. This band appears as doubly magic also in the calculations with widely used NL3 [58] and NLZ [61] parametrizations of the RMF Lagrangian; see Table II. Extensive calculations with the NL3 parametrization (similar to the ones presented in Fig. 22) show that this band become yrast at $I \sim 62\hbar$. The $Z = 53$ ESD shell gap is smaller than 1 MeV only in the NLSH [60] parametrization of the RMF Lagrangian (see Table II). However, it is known that the single-particle energies are not well described in this parametrization [51].

TABLE II. The size of the $Z = 53$ and $N = 58$ ESD shell gaps (in MeV) obtained with different parametrizations of the RMF Lagrangian for the configuration A in ^{111}I at spin $I = 60\hbar$ (rotational frequency $\Omega_x \approx 0.96$ MeV).

	NL1	NL3	NLZ	NLSH
$Z = 53$	1.45	1.25	1.65	0.70
$N = 58$	1.75	1.85	1.60	2.00

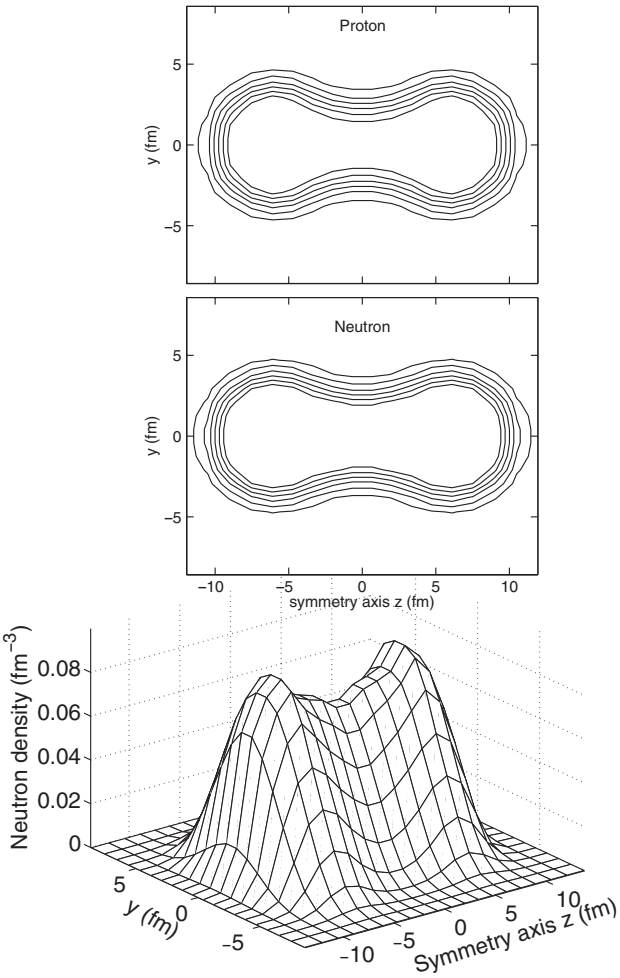

FIG. 21. The same as in Fig. 12 but for yrast megadeformed state in ^{102}Pd at rotational frequency $\Omega_x = 0.95$ MeV. Two top panels show two-dimensional plots of the proton and neutron density distribution.

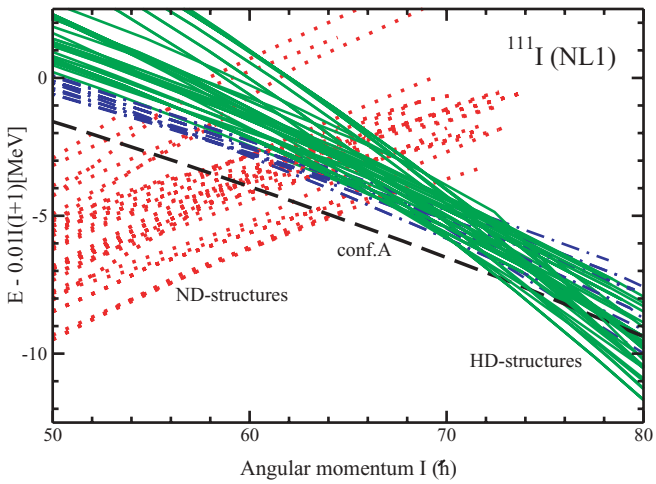

FIG. 22. (Color online) Energies of the calculated configurations relative to a smooth liquid drop reference $AI(I+1)$, with the inertia parameter $A = 0.01$. Normal deformed (ND), SD, and HD configurations are shown by dotted, dot-dashed, and solid lines, respectively. Configuration A is shown by long-dashed line.

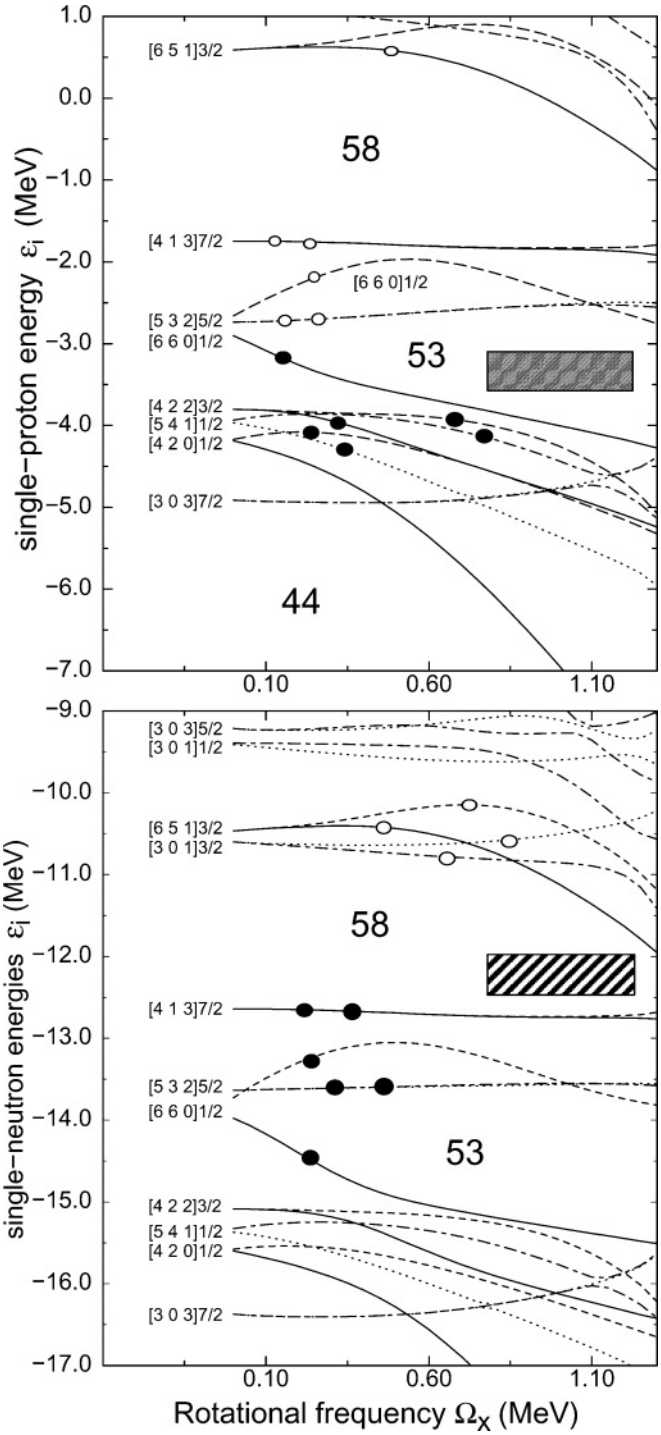

FIG. 23. The same as in Fig. 10 but for the configuration A in ^{111}I. Solid (open) circles indicate the orbitals occupied (emptied). The dashed box indicates the frequency range corresponding to the spin range $I = 50$–$75\hbar$ in this configuration.

One should note, however, that the size of the ESD gaps in the configuration A of ^{111}I is somewhat smaller than the one for the yrast SD band in ^{152}Dy (compare Fig. 22 in the present manuscript with Fig. 3 in Ref. [4]; see also Figs. 4, 11, 12 in Ref. [39] obtained with different parametrizations of the RMF Lagrangian and relevant for ^{151}Tb).

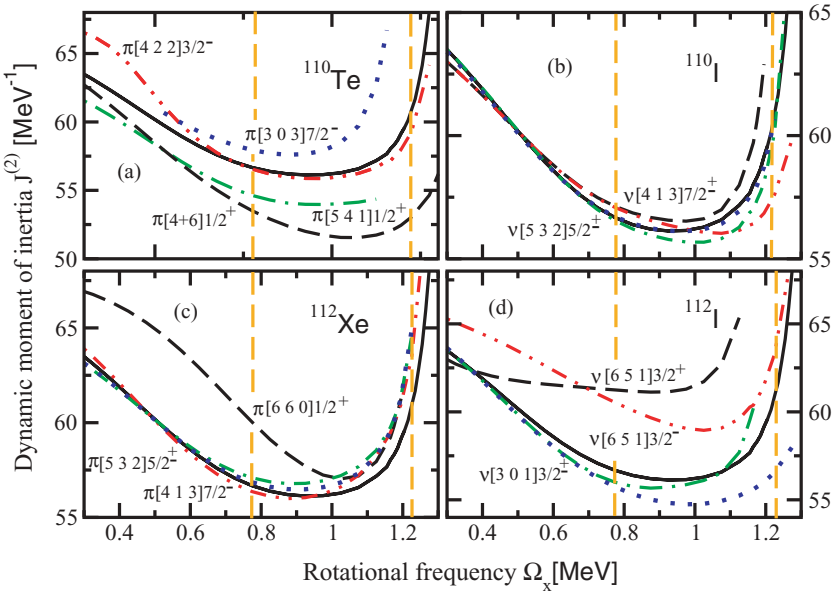

FIG. 24. (Color online) The same as in Fig. 15 but for dynamic moments of inertia $J^{(2)}$ of the configurations used in Fig. 25. Dynamic moments of inertia of the configuration A in ^{111}I are shown by solid line in each panel. Vertical dashed lines indicate the frequency range corresponding to the spin range $I = 50$–$75\hbar$ in the configuration A of ^{111}I. The $\pi[4+6]1/2$ label in (a) indicates the orbital with strong mixing of the $N = 4$ and $N = 6$ shells: this mixing predominantly emerges from the interaction of the $\pi[420]1/2$ and $\pi[660]1/2$ states.

The dynamic moments of inertia of the configuration A in ^{111}I and the configurations in neighboring nuclei are shown in Fig. 24. The increase of $J^{(2)}$ at $\Omega_x \sim 1.2$ MeV is in part due to unpaired band crossing caused by the interaction of the occupied $\nu[413]7/2^-$ and unoccupied $\nu[651]3/2^-$ orbitals (Fig. 23). A centrifugal stretching may also contribute to this increase of $J^{(2)}$. The effect of the occupation of a single-proton (neutron) intruder orbital on the properties of the ESD bands is much more pronounced than that in the HD bands of the nuclei around ^{124}Xe (see Sec. III D); the changes induced into dynamic moment of inertia reach at least 10% of its absolute value for the $\pi[660]1/2^+$ [Fig. 24(c)], $\pi[4+6]1/2^+$ [Fig. 24(a)], $\nu[651]3/2^+$ [Fig. 24(d)], and $\nu[651]3/2^-$ [Fig. 24(d)] orbitals. In a similar way, the effective alignments of these orbitals as well as of the $\pi[541]1/2^+$ orbital show appreciable variations as a function of rotational frequency (see Fig. 25), reaching at least $1\hbar$ in the spin range of interest. This suggests that the configuration assignment based on the effective alignment method will be more reliable in the case of ESD bands as compared with the HD bands in the nuclei around ^{124}Xe (see Sec. III D for a discussion of these methods). Relative properties of the dynamic moments of inertia of two compared bands will also play a complimentary role in the configuration assignment.

V. CONCLUSIONS

For the first time, the hyperdeformation at high spin has been studied in a systematic way within the framework of a fully self-consistent theory: the cranking relativistic mean-field theory. The study covers even-even nuclei in the $Z = 40$–58 part of nuclear chart. The main results can be summarized as follows:

(i) The crossing spins $I_{\rm cr}^{\rm HD}$, at which the HD configurations become yrast, are lower for proton-rich nuclei. This is

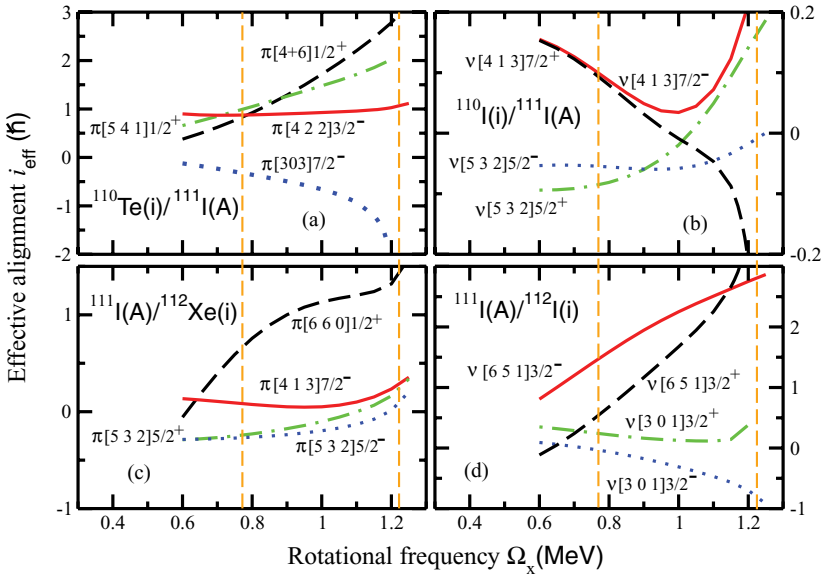

FIG. 25. (Color online) The same as in Fig. 16 but for effective alignments of the single-particle orbitals in the vicinity of the $Z = 53$ and $N = 58$ SD shell gaps (see Fig. 23). The effective alignments are defined with respect to the configuration A in ^{111}I. Vertical dashed lines indicate the frequency range corresponding to the spin range $I = 50$–$75\hbar$ in the configuration A of ^{111}I.

a feature seen in the most of studied isotope chains; by going from the β-stability valley toward the proton drip line one can lower I_{cr}^{HD} by approximately $10\hbar$.

(ii) The density of the HD bands in the spin range where they are yrast or close to yrast is high in the majority of the cases. For such densities, the feeding intensity of an individual HD band will most likely drop below the observational limit of modern experimental facilities. This fact has to be taken into account when planning the experiments for a search of discrete HD bands. Our calculations indicate Cd isotopes and few other nuclei with large shell gaps (see Sec. III E for details) as the best candidates for a search of discrete HD bands. An alternative candidate is the doubly magic extremely superdeformed band in ^{111}I, the deformation of which is only slightly lower than that of the HD bands and which may be observed with existing experimental facilities.

(iii) The high density of the HD bands will most likely favor the observation of the rotational patterns in the form of ridge structures in three-dimensional rotational mapped spectra. The study of these patterns as a function of proton and neutron numbers, which seems to be possible with existing facilities, will provide a valuable information about hyperdeformation at high spin.

(iv) With a very few exceptions, the HD shapes undergo a centrifugal stretching that results in an increase of the values of the transition quadrupole Q_t and mass hexadecapole Q_{40} moments as well as the dynamic moments of inertia $J^{(2)}$ with increasing rotational frequency. The kinematic moments of inertia $J^{(1)}$ show very small variations in the frequency range of interest. These are general features of the HD bands that distinguish them from the normal and superdeformed bands. Such features have not been seen before in the calculations without pairing. In unpaired regime, the Q_t, $J^{(2)}$, and $J^{(1)}$ values decrease with rotational frequency in the SD configurations; the only exceptions are the regions of unpaired bands crossings.

(v) The individual properties of the single-particle orbitals are not lost at HD. In the future, they will allow the assignment of the configurations to the HD bands using the relative properties of different bands. Such methods of configuration assignment were originally developed for superdeformation. In contrast to the case of SD, our analysis in the $A \sim 125$ mass region shows that only simultaneous application of the methods based on effective alignments and relative transition quadrupole moments by comparing experimental and theoretical $(i_{\rm eff}, \Delta Q_t)$ values will lead to a reliable configuration assignment for the HD bands. Moreover, additional information on the structure of the HD bands will be obtained from the band crossing features; the cases of strong interaction of the bands in unpaired regime at HD will be more common as compared with the situation at SD.

The physics of hyperdeformation at high spin is also defined by the fission barriers; the competition with fission certainly makes the population of the HD states difficult. It is an important issue that, however, goes beyond the scope of the current manuscript. It is likely that the fission barriers are small or nonexistent at the spins around 80–$90\hbar$ in some of the studied nuclei; the observation of the HD bands then will not be possible in these systems. This problem definitely deserves a deeper attention; the study of the fission barriers at high spin typical for HD within the framework of the cranked relativistic Hartree-Bogoliubov theory is in its initial stage and the results will be presented in a forthcoming article.

ACKNOWLEDGMENTS

The help of C. W. Jang and J. Begnaud in performing numerical calculations is highly appreciated. The work was supported by the U.S. Department of Energy under grant DE-FG02-07ER41459. Stimulating discussions with Robert Janssens are gratefully acknowledged.

[1] P. J. Twin, B. M. Nyakó, A. H. Nelson, J. Simpson, M. A. Bentley, H. W. Cranmer-Gordon, P. D. Forsyth, D. Howe, A. R. Mokhtar, J. D. Morrison, J. F. Sharpey-Schafer, and G. Sletten, Phys. Rev. Lett. **57**, 811 (1986).
[2] B. Singh, R. Zywina, and R. B. Firestone, Nucl. Data Sheets **97**, 241 (2002).
[3] C. Baktash, B. Haas, and W. Nazarewicz, Annu. Rev. Nucl. Part. Sci. **45**, 485 (1995).
[4] A. V. Afanasjev, J. König, and P. Ring, Nucl. Phys. **A608**, 107 (1996).
[5] J. Dudek, K. Pomorski, N. Schunck, and N. Dubray, Eur. Phys. J. A **20**, 15 (2004).
[6] A. Bohr and B. Mottelson, *Nuclear Structure* (Benjamin, New York, 1975), Vol. II.
[7] R. Bengtsson, I. Ragnarsson, S. Åberg, A. Gyurkovich, A. Sobiczewski, and K. Pomorski, Nucl. Phys. **A473**, 77 (1987).
[8] R. R. Chasman, Phys. Lett. **B302**, 134 (1993).
[9] J. Dudek, *The Variety of Nuclear Shapes*, edited by J. D. Garrett (World Scientific, Singapore, 1988), p. 195.
[10] S. Åberg, Nucl. Phys. **A557**, 17c (1993).
[11] S. Ćwiok, W. Nazarewicz, J. X. Saladin, W. Płóciennik, and A. Johnson, Phys. Lett. **B322**, 304 (1994).
[12] T. Werner and J. Dudek, At. Data Nucl. Data Tables **59**, 1 (1995).
[13] R. R. Chasman and L. M. Robledo, Phys. Lett. **B351**, 18 (1995).
[14] L. Jönsson and S. Åberg, Nucl. Phys. **A627**, 53 (1997).
[15] R. R. Chasman, Phys. Rev. C **64**, 024311 (2001).
[16] J. L. Egido, L. M. Robledo, and R. R. Chasman, Phys. Lett. **B393**, 13 (1997).
[17] A. Staszczak, J. Dobaczewski, and W. Nazarewicz, Int. J. Mod. Phys. E **16**, 310 (2007).
[18] S. Hilaire and M. Girod, Eur. Phys. J. A **33**, 237 (2007).
[19] K. Rutz, J. A. Maruhn, P.-G. Reinhard, and W. Greiner, Nucl. Phys. **A590**, 680 (1995).
[20] A. V. Afanasjev and S. Frauendorf, Phys. Rev. C **72**, 031301(R) (2005).
[21] T. Inakura, S. Mizutori, M. Yamagami, and K. Matsuyanagi, Nucl. Phys. **A710**, 261 (2002).

[22] V. V. Pashkevich, Nucl. Phys. **A169**, 275 (1971).
[23] P. Möller and J. R. Nix, *Physics and Chemistry of Fission 1973* (IAEA, Vienna, 1974), Vol. 1, p. 103.
[24] A. Krasznahorkay, M. Hunyadi, M. N. Harakeh, M. Csatlós, T. Faestermann, A. Gollwitzer, G. Graw, J. Gulyás, D. Habs, R. Hertenberger, H. J. Maier, Z. Máté, D. Rudolph, P. Thirolf, J. Timár, and B. D. Valnion, Phys. Rev. Lett. **80**, 2073 (1998).
[25] C. M. Brink, H. Friedrich, A. Weiguny, and C. W. Wong, Phys. Lett. **B33**, 143 (1970).
[26] A. Galindo-Uribarri, H. R. Andrews, G. C. Ball, T. E. Drake, V. P. Janzen, J. A. Kuehner, S. M. Mullins, L. Persson, D. Prévost, D. C. Radford, J. C. Waddington, D. Ward, and R. Wyss, Phys. Rev. Lett. **71**, 231 (1993).
[27] G. Viesti, M. Lunardon, D. Bazzacco, R. Burch, D. Fabris, S. Lunardi, N. H. Medina, G. Nebbia, C. Rossi-Alvarez, G. de Angelis, M. De Poli, E. Fioretto, G. Prete, J. Rico, P. Spolaore, G. Vedovato, A. Brondi, G. La Rana, R. Moro, and E. Vardaci, Phys. Rev. C **51**, 2385 (1995).
[28] R. M. Clark, P. Fallon, A. Görgen, M. Cromaz, M. A. Deleplanque, R. M. Diamond, G. J. Lane, I. Y. Lee, A. O. Macchiavelli, R. G. Ramos, F. S. Stephens, C. E. Svensson, K. Vetter, D. Ward, M. P. Carpenter, R. V. F. Janssens, and R. Wadsworth, Phys. Rev. Lett. **87**, 202502 (2001).
[29] A. Görgen, R. M. Clark, P. Fallon, M. Cromaz, M. A. Deleplanque, R. M. Diamond, G. J. Lane, I. Y. Lee, A. O. Macchiavelli, R. G. Ramos, F. S. Stephens, C. E. Svensson, K. Vetter, D. Ward, M. P. Carpenter, R. V. F. Janssens, and R. Wadsworth, Phys. Rev. C **65**, 027302 (2002).
[30] N. Schunck, J. Dudek, and B. Herskind, Phys. Rev. C **75**, 054304 (2007).
[31] B. Herskind, G. B. Hagemann, G. Sletten, Th. Døssing, C. Rønn Hansen, N. Schunck, S. Ødegård, H. Hübel, P. Bringel, A. Bürger, A. Neusser, A. K. Singh, A. Al-Khatib, S. B. Patel, A. Bracco, S. Leoni, F. Camera, G. Benzoni, P. Mason, A. Paleni, B. Million, O. Wieland, P. Bednarczyk, F. Azaiez, Th. Byrski, D. Curien, O. Dakov, G. Duchene, F. Khalfallah, B. Gall, L. Piqeras, J. Robin, J. Dudek, N. Rowley, B. M Nyakó, A. Algora, Z. Dombradi, J. Gal, G. Kalinka, D. Sohler, J. Molnár, J. Timár, L. Zolnai, K. Juhász, N. Redon, F. Hannachi, J. N. Scheurer, J. N. Wilson, A. Lopez-Martens, A. Korichi, K. Hauschild, J. Roccaz, S. Siem, P. Fallon, I. Y. Lee, A. Görgen, A. Maj, M. Kmiecik, M. Brekiesz, J. Styczen, K. Zuber, J. C. Lisle, B. Cederwall, K. Lagergren, A. O. Evans, G. Rainovski, G. De Angelis, G. La Rana, R. Moro, W. Gast, R. M. Lieder, E. Podsvirova, H. Jäger, C. M. Petrache, and D. Petrache, Phys. Scr., T **125**, 108 (2006).
[32] B. M. Nyakó, F. Papp, J. Gal, J. Molnár, J. Timár, A. Algora, Zs. Dombrádi, G. Kalinka, L. Zolnai, K. Juhász, A. K. Singh, H. Hüebel, A. Al-Khatib, P. Bringel, A. Büerger, A. Neusser, G. Schöenwasser, B. Herskind, G. B. Hagemann, C. R. Hansen, G. Sletten, J. N. Scheurer, F. Hannachi, M. Kmiecik, A. Maj, J. Styczeń, K. Zuber, K. Hauschild, A. Korichi, A. Lopez-Martens, J. Roccaz, S. Siem, P. Bednarczyk, Th. Byrski, D. Curien, O. Dorvaux, G. Ducheńe, B. Gall, F. Khalfallah, I. Piqueras, J. Robin, S. B. Patel, A. O. Evans, G. Rainovski, A. Airoldi, G. Benzoni, A. Bracco, F. Camera, B. Million, P. Mason, A. Paleni, R. Sacchi, O. Wieland, G. La Rana, R. Moro, C. M. Petrache, D. Petrache, G. De Angelis, P. Fallon, I.-Y. Lee, J. C. Lisle, B. Cederwall, K. Lagergren, R. M. Lieder, E. Podsvirova, W. Gast, H. Jäeger, N. Redon, and A. Göergen, Acta Phys. Pol. B **36**, 1033 (2005).
[33] H. Hübel, Acta Phys. Pol. B **36**, 1015 (2005).
[34] D. R. LaFosse, D. G. Sarantites, C. Baktash, P.-F. Hua, B. Cederwall, P. Fallon, C. J. Gross, H.-Q. Jin, M. Korolija, I. Y. Lee, A. O. Macchiavelli, M. R. Maier, W. Rathbun, D. W. Stracener, and T. R. Werner, Phys. Rev. Lett. **74**, 5186 (1995).
[35] D. R. LaFosse, D. G. Sarantites, C. Baktash, S. Asztalos, M. J. Brinkman, B. Cederwall, R. M. Clark, M. Devlin, P. Fallon, C. J. Gross, H.-Q. Jin, I. Y. Lee, F. Lerma, A. O. Macchiavelli, R. MacLeod, D. Rudolph, D. W. Stracener, and C.-H. Yu, Phys. Rev. C **54**, 1585 (1996).
[36] J. N. Wilson, S. J. Asztalos, R. A. Austin, B. Busse, R. M. Clark, M. A. Deleplanque, R. M. Diamond, P. Fallon, S. Flibotte, G. Gervais, D. S. Haslip, I. Y. Lee, R. Kruecken, A. O. Macchiavelli, R. W. MacLeod, J. M. Nieminen, G. J. Schmid, F. S. Stephens, O. Stezowski, C. E. Svensson, K. Vetter, and J. C. Waddington, Phys. Rev. C **56**, 2502 (1997).
[37] T. Bengtsson, I. Ragnarsson, and S. Åberg, Phys. Lett. **B208**, 39 (1988).
[38] I. Ragnarsson, Nucl. Phys. **A557**, 167c (1993).
[39] A. V. Afanasjev, G. Lalazissis, and P. Ring, Nucl. Phys. **A634**, 395 (1998).
[40] W. Satuła, J. Dobaczewski, J. Dudek, and W. Nazarewicz, Phys. Rev. Lett. **77**, 5182 (1996).
[41] M. Matev, A. V. Afanasjev, J. Dobaczewski, G. A. Lalazissis, and W. Nazarewicz, Phys. Rev. C **76**, 034304 (2007).
[42] B. D. Serot and J. D. Walecka, Adv. Nucl. Phys. **16**, 1 (1986).
[43] P.-G. Reinhard, Rep. Prog. Phys. **52**, 439 (1989).
[44] D. Vretenar, A. V. Afanasjev, G. Lalazissis, and P. Ring, Phys. Rep. **409**, 101 (2005).
[45] W. Koepf and P. Ring, Nucl. Phys. **A493**, 61 (1989).
[46] W. Koepf and P. Ring, Nucl. Phys. **A511**, 279 (1990).
[47] J. König and P. Ring, Phys. Rev. Lett. **71**, 3079 (1993).
[48] A. V. Afanasjev and S. Frauendorf, Phys. Rev. C **71**, 064318 (2005).
[49] A. V. Afanasjev, I. Ragnarsson, and P. Ring, Phys. Rev. C **59**, 3166 (1999).
[50] N. Schunck (private communication, 2008).
[51] A. V. Afanasjev, T. L. Khoo, S. Frauendorf, G. A. Lalazissis, and I. Ahmad, Phys. Rev. C **67**, 024309 (2003).
[52] A. V. Afanasjev and P. Ring, Phys. Rev. C **62**, 031302(R) (2000).
[53] M. Samyn, S. Goriely, and J. M. Pearson, Phys. Rev. C **72**, 044316 (2005).
[54] W. Nazarewicz and I. Ragnarsson, in *Handbook on Nuclear Properties*, edited by D. N. Poenaru and W. Greiner (Claredon Press, Oxford, 1996), p. 80.
[55] A. V. Afanasjev, D. B. Fossan, G. J. Lane, and I. Ragnarsson, Phys. Rep. **322**, 1 (1999).
[56] P.-G. Reinhard, M. Rufa, J. Maruhn, W. Greiner, and J. Friedrich, Z. Phys. A **323**, 13 (1986).
[57] G. A. Lalazissis and P. Ring, Phys. Lett. **B427**, 225 225 (1998).
[58] G. A. Lalazissis, J. König, and P. Ring, Phys. Rev. C **55**, 540 (1997).
[59] M. Devlin, A. V. Afanasjev, R. M. Clark, D. R. LaFosse, I. Y. Lee, F. Lerma, A. O. Macchiavelli, R. W. MacLeod, I. Ragnarsson, P. Ring, D. Rudolph, D. G. Sarantites, and P. G. Thirolf, Phys. Rev. Lett. **82**, 5217 (1999).
[60] M. M. Sharma, M. A. Nagarajan, and P. Ring, Phys. Lett. **B312**, 377 (1993).
[61] M. Rufa, P.-G. Reinhard, J. A. Maruhn, W. Greiner, and M. R. Strayer, Phys. Rev. C **38**, 390 (1988).

[62] G. A. Lalazissis, T. Nikšić, D. Vretenar, and P. Ring, Phys. Rev. C **71**, 024312 (2005).
[63] F. G. Kondev, M. A. Riley, R. V. F. Janssens, J. Simpson, A. V. Afanasjev, I. Ragnarsson, I. Ahmad, D. J. Blumenthal, T. B. Brown, M. P. Carpenter, P. Fallon, S. M. Fischer, G. Hackman, D. J. Hartley, C. A. Kalfas, T. L. Khoo, T. Lauritsen, W. C. Ma, D. Nisius, J. F. Sharpey-Schafer, and P. G. Varmette, Phys. Lett. **B437**, 35 (1998).
[64] T. Lauritsen, M. P. Carpenter, T. Døssing, P. Fallon, B. Herskind, R. V. F. Janssens, D. G. Jenkins, T. L. Khoo, F. G. Kondev, A. Lopez-Martens, A. O. Macchiavelli, D. Ward, K. S. Abu Saleem, I. Ahmad, R. Clark, M. Cromaz, J. P. Greene, F. Hannachi, A. M. Heinz, A. Korichi, G. Lane, C. J. Lister, P. Reiter, D. Seweryniak, S. Siem, R. C. Vondrasek, and I. Wiedenhöver, Phys. Rev. Lett. **88**, 042501 (2002).
[65] E. S. Paul, P. T. W. Choy, C. Andreoiu, A. J. Boston, A. O. Evans, C. Fox, S. Gros, P. J. Nolan, G. Rainovski, J. A. Sampson, H. C. Scraggs, A. Walker, D. E. Appelbe, D. T. Joss, J. Simpson, J. Gizon, A. Astier, N. Buforn, A. Prévost, N. Redon, O. Stézowski, B. M. Nyakó, D. Sohler, J. Timár, L. Zolnai, D. Bazzacco, S. Lunardi, C. M. Petrache, P. Bednarczyk, D. Curien, N. Kintz, and I. Ragnarsson, Phys. Rev. C **71**, 054309 (2005).
[66] H. Hübel (private communication, 2008).
[67] R. Wyss and W. Satuła, Phys. Lett. **B351**, 393 (1995).
[68] A. V. Afanasjev, P. Ring, and J. König, Nucl. Phys. **A676**, 196 (2000).
[69] P. Ring and P. Schuck, *The Nuclear Many-Body Problem* (Springer Verlag, Heidelberg, 1980).
[70] A. V. Afanasjev, I. Ragnarsson, and P. Ring, Phys. Rev. C **59**, 3166 (1999).
[71] S. T. Clark, G. Hackman, R. V. F. Janssens, R. M. Clark, P. Fallon, S. N. Floor, G. J. Lane, A. O. Macchiavelli, J. Norris, S. J. Sanders, and C. E. Svensson, Phys. Rev. Lett. **87**, 172503 (2001).
[72] R. W. Laird, F. G. Kondev, M. A. Riley, D. E. Archer, T. B. Brown, R. M. Clark, M. Devlin, P. Fallon, D. J. Hartley, I. M. Hibbert, D. T. Joss, D. R. LaFosse, P. J. Nolan, N. J. O'Brien, E. S. Paul, J. Pfohl, D. G. Sarantites, R. K. Sheline, S. L. Shepherd, J. Simpson, R. Wadsworth, M. T. Matev, A. V. Afanasjev, J. Dobaczewski, G. A. Lalazissis, W. Nazarewicz, and W. Satuła, Phys. Rev. Lett. **88**, 152501 (2002).
[73] G. Hackman, R. Wadsworth, D. S. Haslip, R. M. Clark, J. Dobaczewski, J. Dudek, S. Flibotte, K. Hauschild, I. M. Hibbert, I.-Y. Lee, S. M. Mullins, A. O. Macchiavelli, S. Pilotte, A. T. Semple, I. Thorslund, J. Timar, P. Vaska, J. C. Waddington, and L. Walker, Phys. Rev. C **52**, R2293 (1995).
[74] A. V. Afanasjev and P. Ring, Nucl. Phys. **A654**, 647c (1999).
[75] I. Ragnarsson, Phys. Lett. **B264**, 5 (1991).